APPROVAL PAGE FOR GRADUATE THESIS OR PROJECT

GS-13

SUBMITTED IN PARTIAL FULFILLMENT OF REQUIREMENTS FOR DEGREE OF MASTER OF SCIENCE AT CALIFORNIA STATE UNIVERSITY, LOS ANGELES BY

Omar Moreno
Candidate

Physics
Field of Concentration

TITLE: Measurement of the Analyzing Power for the Reactions $\boldsymbol{p}+CH_2 \rightarrow X$ at a Proton Momentum of 2.2032 GeV/c

APPROVED:

Konrad A. Aniol, PhD Faculty Member	Signature
Martin B. Epstein, PhD Faculty Member	Signature
Demetrius J. Margaziotis, PhD Faculty Member	Signature
Edward Rezayi, PhD Department Chairperson	Signature

DATE: September 9, 2009

MEASUREMENT OF THE ANALYZING POWER FOR THE REACTION $\vec{p}$+$CH_2 \rightarrow X$ AT A PROTON MOMENTUM OF 2.2032 GeV/c

A Thesis

Presented to

The Faculty of the Department of Physics and Astronomy

California State University, Los Angeles

In Partial Fulfillment

of the Requirements for the Degree

Master of Science

By

Omar Moreno

September 2009

ACKNOWLEDGEMENTS

The completion of this thesis was due in large part to the guidance and support that I received from the G_E^p-III collaboration at the Thomas Jefferson National Accelerator Facility as well as the California State University, Los Angeles Nuclear Physics Group. I am greatful that the G_E^p-III spokespersons, Edward Brash[1], Mark Jones[2], Charles Perdrisat[3] and Vina Punjabi[4] allowed me to take part in such a breakthrough experiment. Specifically, I want to give thanks to Mark Jones and Charles Perdrisat for taking the time to mentor me and instill in me valuable knowledge that I will continue to use in the future. I would also like to thank the G_E^p-III graduate (Wei Lou, Mehdi Mezianne, and Andrew Puckett) and post-doctoral (Lubomir Penchev and Frank Wesselmann) students for their guidance through the construction of the detectors and the analysis.

A large part of the experimental nuclear physics knowledge that I have gained over the past two years has come from my adviser, Professor Konrad Aniol. His excitement on the subject matter was visible ever since I first joined the group, and this allowed me to grow in the field of nuclear physics. I would also like to thank the rest of my thesis committee members Professor Martin Epstein, Professor Demetrius Margaziotis, and Professor Edward Rezayi for taking the time to review my thesis and provide helpful feedback.

The work in this thesis would not have been possible without the support provided by the Louise Stokes Alliance for Minority Participation - Bridge to the Doctorate

[1]Christopher Newport University, Newport News, VA
[2]Thomas Jefferson National Accelerator Facility, Newport News, VA
[3]College of William and Mary, Williamsburg, VA
[4]Norfolk State University, Norfolk, VA

(LSAMP-BD) program and Margaret Jefferson. The program allowed me to fully dedicate myself to my studies and allowed me to work at my full potential.

I would also like to thank my family Jose Moreno, Olga Moreno, Patricia Moreno and my future physicist Joseph Alexander Moreno. To my father and mother, you have instilled in me (through my observation of both of you) two qualities that allowed me to succeed in the past couple of years: always pursue my goals to the best of my ability and never give up no matter what the situation. To my sister, I hope to see you in my position soon so work hard and remember that I will always be here to support you. To Joseph, I hope that one day you will be able to read this and enjoy it (and hopefully point out some errors).

Finally I want to thank Monica Delgado for supporting me and encouraging me to work hard these past couple of years. I am glad that I was able to meet another person who is interested in making a great difference in their field, and I am confident that the completion of our theses is just the beginning of the many successes we are going to have.

The funding for this program is provided by National Science Foundation under Grant # HRD-00331537 and the CSU Chancellor's Office.

ABSTRACT

Measurement of the Analyzing Power for the Reaction $\vec{p}$+$CH_2 \rightarrow X$ at a Proton Momentum of 2.2032 GeV/c

By

O. Moreno

This thesis will present the analyzing power measurement for the reaction $\vec{p}$+$CH_2 \rightarrow X$ at a proton momentum of 2.2032 GeV/c. The azimuthal angular distribution of polarized protons in the CH_2 analyzer is sensitive to the strength of the spin-orbit coupling or analyzing power of the reaction $\vec{p}$+$CH_2 \rightarrow X$. The analyzing powers for a subset of data identified by an electromagnetic calorimeter to be protons will also be presented. An improvement in the analyzing power measurement was observed when using the calorimeter to identify protons. Finally, the Sachs form factor measurement for the $Q^2 = 2.733$ GeV^2 point will also be presented.

Recoiling protons produced in the $\vec{e}+p \rightarrow e'+\vec{p}$ reaction are polarized. The recoil polarization technique, used to measure the ratio of the electromagnetic form factors G_E^p/G_M^p of the proton, involves measuring the induced polarization of the proton with the use of the Focal Plane Polarimeter (FPP). The FPP is composed of two blocks of $(CH_2)_n$ with pairs of drift chambers interleaved.

Measurement of the analyzing power to a high degree of accuracy is important since it will significantly reduce the error in the electromagnetic form factor measurement. Furthermore, knowledge of the analyzing power can be used to optimize the characteristics of the FPP for future experiments.

Insight into the electric charge and magnetic dipole moment distributions in the proton can be used to test Quantum Chromodynamics calculations of the proton's

quark constituents. The G_E^p-III experiment at the Thomas Jefferson National Accelerator Facility has made measurements of the ratio of the Sachs form factors, G_E^p/G_M^p up to a four momentum transfer of $Q^2 = 9.00$ GeV^2 via the recoil polarization technique. The work described in this thesis supports this experimental program for the $Q^2 = 2.733$ GeV^2 point.

TABLE OF CONTENTS

LIST OF TABLES

LIST OF FIGURES

Chapter 1

Introduction and Overview

In 1928, Paul A. M. Dirac formulated a relativistic quantum mechanical wave equation which was thought to describe the dynamics of all spin $\frac{1}{2}$ particles. At the time this included the proton, which had been observed by Ernest Rutherford in 1918, and would later include the neutron which was not observed until 1932 by James Chadwick [1].

In accordance with Dirac's formulation, the magnetic moment of all spin $\frac{1}{2}$ particles is given by

$$\mu = -g\frac{q}{2mc}\left|\vec{S}\right| \tag{1.1}$$

where m is the mass of the particle, q its charge, g is a constant, c is the speed of light and S is its spin. The dependence of the magnetic moment on charge would then imply that the neutron should have a null magnetic moment due to its neutrality; a hypothesis which was disproven in 1939 by Luis W. Alvarez and Felix Bloch [2]. Furthermore, in 1933, O. Stern measured the magnetic moment of the proton to be 2.79 times greater than that predicted by Dirac theory [3]. These continued disagreements with Dirac's formulation were the first indications that the proton and neutron were not fundamental particles and further new physics would be required.

With the development of particle detectors in the 1950's, physicist began to observe a throng of new particles. It soon became apparent that these "hadrons", as they came to be called, could not all be fundamental. In 1964, Murray Gell-Mann and George Zweig proposed a resolution which described the properties of most of these particles if they were assumed to be composed of three fundamental particles, dubbed

quarks, of non-integral charge[4, 5]. Verification of their hypothesis came in 1969 at the Stanford Linear Accelerator Center (SLAC) in an experiment which saw electrons deeply scattered from protons (SLAC) [6, 7]. In turn, Gell-Mann and Zweig's theory would eventually evolve into Quantum Chromodynamics which describes the quarks to have 6 flavors that interact via the exchange of gluons. With the discovery of the top quark in 1995 by the CDF and DØ collaborations at FermiLab [8, 9], all of the quarks have now been observed. Their properties are listed on Table 1.1.

Table 1.1: The properties of all quarks. Note that q represents charge in units of the electron charge and j is the total spin angular momentum in units of $\hbar$.

Name (Symbol)	Mass (MeV/c^2)	q (e)	j ($\hbar$)
Up (u)	1.5 to 3.3	+2/3	1/2
Down (d)	3.5 to 6.0	-1/3	1/2
Charm (c)	1,270	+2/3	1/2
Strange (s)	104	-1/3	1/2
Top (t)	171,200 $\pm$ 2,100	+2/3	1/2
Bottom (b)	4,200	-1/3	1/2

Even though it is now clear that the net flavor structure of the proton is composed of two up quarks and one down quark, many mysteries still remain. One such problem is the distribution of the electric charge and the magnetic dipole moment of the proton. Furthermore, it is still unclear how exactly the proton strongly interacts with other nucleons. The G_E^p-III (E04-108) experiment has addressed both issues by measuring the Sachs form factor ratio G_E^p/G_M^p up to a four momentum transfer squared of $Q^2 = 9.00$ GeV^2. The form factors are directly related to the electric charge and magnetic dipole moment distributions of the proton through a Fourier transform. The form factors were then used to extract the strength of the spin orbit coupling or

analyzing power for the reaction $\vec{p}$+(CH_2)$\rightarrow X$.

The work described in this thesis supports the experimental program for the $Q^2 = 2.733\ \mathrm{GeV}^2$ point. First, the analyzing power for the reaction p+$CH_2 \rightarrow X$ at a proton momentum of 2.2032 GeV/c will be presented for several detector conditions. Next, it will be shown that the analyzing power can be improved by identifying the final state proton using an electromagnetic calorimeter. Finally, the extracted form factor ratio G_E^p/G_M^p will be compared to previous measurements that were made using the recoil polarization technique.

1.1 Theoretical Formalism

The structure of the proton can be best probed using the electromagnetic interaction present in electron-proton (ep) scattering. This is due in part to the small size of the electromagnetic coupling constant, $\alpha = 1/137$, allowing any physical process to be accurately described by the leading orders of perturbation theory. Furthermore, since the electron vertex is highly understood from Quantum Electrodynamics (QED) it is expected that only the hadronic vertex will provide any new physics regarding the proton structure. Unfortunately, the choice of probe also limits the exploration of the proton structure to the electromagnetic regime, neglecting the gluons which are an important piece of the puzzle. In what follows, a formal description detailing the extraction of the form factors from ep scattering will be given.

1.1.1 ep Scattering

Let us begin our formal discussion of ep scattering by considering a polarized electron of four momentum $p = (E_e, \vec{p})$ which interacts with a proton of four momentum $k = (E_p, \vec{k})$ via the exchange of a virtual photon of four momentum $q = (\omega, \vec{q})$. Using

the Feynman rules, the elastic ep scattering amplitude can be written from the first

Figure 1.1: First order Feynman diagram describing elastic electron-proton scattering in the single photon exchange or Born approximation.

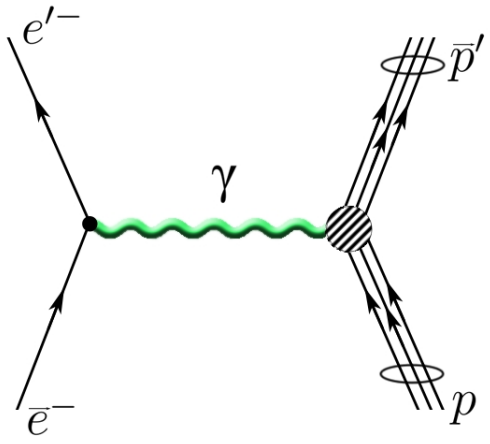

order Feynman diagram shown on Figure 1.1 as [10]

$$i\mathcal{M} = [ie\bar{v}(k')\Gamma^{\mu}(k',k)\,v(k)]\,\frac{-ig_{\mu\nu}}{q^2}\,[ie\bar{u}(p')\gamma^{\nu}u(p)] \tag{1.2}$$

$$= \frac{-i}{q^2}\,[ie\bar{v}(k')\Gamma^{\mu}(k',k)\,v(k)]\,[ie\bar{u}(p')\gamma_{\mu}u(p)] \tag{1.3}$$

where $\gamma^{\nu} = (\gamma^0, \gamma^1, \gamma^2, \gamma^3)$ is a four-vector whose components are the Dirac γ matrices, e is the charge of the electron, $g_{\mu\nu}$ is the Minkowski metric, and q^2 is the four momentum transfer squared defined as[5]

$$q^2 = \left(\omega^2 - \vec{q}^2\right) = -Q^2. \tag{1.4}$$

A full description of the γ-matrices and the Minkowski metric are given in Appendix

[5]For scattering in the space-like region, q^2 is always negative. The positive q^2 regime is accessible through processes such a electron-positron annihilation to $p\bar{p}$.

A. Here,the Dirac spinors $u(p)/u(p')$ $(v(k)/v(k'))$ correspond to the initial/final electron (proton), respectively. They enter the plane-wave solutions of the form

$$\psi^{\pm}(x) = u(p)e^{\mp ip_\mu x^\mu} \tag{1.5}$$

which satisfy the free particle Dirac equation

$$(-i\gamma^\mu \partial_\mu - m)\psi(x) = 0. \tag{1.6}$$

It must be noted that $u(p)$ can be replaced with any of the spinors of equation (1.2). Here p and x are the four momentum and space-time vector position of the particle, respectively.

Unlike the electron current $j_\mu = ie\bar{u}(p')\gamma_\mu u(p)$ which is well understood from Quantum Electrodynamics (QED), the hadronic vertex cannot be derived in the context of Dirac's theory due to the proton structure. Instead, it can be deduced to have the form

$$\Gamma^\mu = \gamma^\mu F_1(q^2) + \frac{i\sigma^{\mu\nu}q_\nu}{2m_p}\kappa F_2(q^2) \tag{1.7}$$

by realizing that Γ^μ is a second rank tensor which can only depend on k, k', and γ^ν in order to remain relativistically invariant and satisfy current conservation [11]. Here, $\sigma^{\mu\nu} = \frac{i}{2}[\gamma^\mu, \gamma^\nu]$, κ is the anomalous magnetic moment of the proton and $F_1(q^2)$ and $F_2(q^2)$, or equivalently, $F_1(Q^2)$ and $F_2(Q^2)$, are the Dirac and Pauli form factors, respectively. The Pauli form factor is said to describe the helicity preserving part of the elastic scattering while the Dirac form factor describes the helicity flipping part.

They are normalized to their values at $Q^2 = 0$ which are

$$F_1(0) = 1 \text{ and } F_2(0) = \kappa. \tag{1.8}$$

1.1.2 Sachs Form Factors

It is of convenience to recast the hadronic vertex (1.7) in terms of the Sachs form factors defined as [11]

$$G_E(Q^2) = F_1 - \tau\kappa F_2 \tag{1.9}$$

and

$$G_M(Q^2) = F_1 + \kappa F_2 \tag{1.10}$$

where τ is a kinematic factor which is equal to

$$\tau = \frac{Q^2}{4m^2}. \tag{1.11}$$

At $Q^2 = 0$ the Sachs form factors of the proton reduce to the electric charge and magnetic moment of the proton

$$G_E^p(0) = 1 \text{ and } G_M^p(0) = \mu_p \tag{1.12}$$

where $\mu_p = 2.79$ is the magnetic moment of the proton.

The Sachs form factors have simple interpretations as the Fourier transform of the electric charge and magnetization densities in the Breit frame[6]. However, because the Breit frame varies with each Q^2, the electromagnetic densities are dependent on the

[6]In the Breit frame the initial and final proton momentum are equal and opposite.

frame. In order to resolve this issue, Kelly introduced the intrinsic form factors which are the Fourier transforms of the electromagnetic densities in the nucleon rest frame and are related to the Sachs form factors through a relativistic prescription. The electric charge and magnetization densities in the nucleon rest frame are then extracted by Kelly using the available Sachs form factor data[12].

The advantage of using the Sachs form factors becomes apparent in the proton current as described in the Breit frame. In this frame of reference the time and space components of the proton current can be expressed exclusively in terms of the electric or magnetic form factors, respectively, as [13]

$$\begin{aligned} \mathcal{J}^0 &= ie2m\chi'^{\dagger}\chi G_E \\ \vec{\mathcal{J}} &= -e\chi'^{\dagger}(\vec{\sigma}\times\vec{q}_b)\chi G_M. \end{aligned} \tag{1.13}$$

Here, χ is a two component spinor, normalized to $\chi\chi^{\dagger}$, related to the Dirac spinors as

$$u(p) = \begin{pmatrix} \sqrt{p\cdot\sigma}\chi \\ \sqrt{p\cdot\bar{\sigma}}\chi \end{pmatrix}.$$

It must once again be noted that $u(p)$ can be replaced by any of the spinors of equation (1.2).

1.1.3 Rosenbluth Cross Section

There are two methods commonly used to measure the Sachs form factors: the Rosenbluth separation technique and the recoil polarization technique. The former requires knowledge of the elastic *ep* scattering cross section which can be written in

the Lab frame as

$$\frac{d\sigma}{d\Omega_e} = \frac{|\mathcal{M}|^2}{64\pi}\frac{1}{m_p^2}\left(\frac{E_e'}{E_e}\right)^2. \tag{1.14}$$

Here, $|\mathcal{M}|^2$ is the ep scattering amplitude, m_p is the mass of the proton, Ω_e is the solid angle in which the electron scatters and E_e' and E_e are the final and initial energies of the electron, respectively.

The scattering amplitude can be calculated in terms of G_E^p and G_M^p by using the leptonic and hadronic currents derived above

$$|\mathcal{M}|^2 = \left[\mathcal{J}^\mu \frac{-i}{q^2} j_\mu\right]\left[\mathcal{J}^\nu \frac{-i}{q^2} j_\nu\right]^* \tag{1.15}$$

$$= \left(\frac{1}{q^2}\right)^2 \left[\mathcal{J}^\mu \mathcal{J}^{\nu *}\right]\left[j_\mu j_\nu^*\right]. \tag{1.16}$$

Defining the leptonic and hadronic tensors as

$$W^{\mu\nu} = \frac{1}{e^2}\mathcal{J}^\mu \mathcal{J}^{\nu *} \tag{1.17}$$

$$L_{\mu\nu} = \frac{1}{e^2} j_\mu j_\nu^* \tag{1.18}$$

the scattering amplitude may be rewritten as

$$|\mathcal{M}|^2 = \left(\frac{e^2}{q^2}\right)^2 W^{\mu\nu} L_{\mu\nu}. \tag{1.19}$$

Explicit calculation of equation (1.19) yields the scattering amplitude in its final form

$$|\mathcal{M}|^2 = \left(\frac{e^2}{Q^2}\right)^2 4m_p^2 Q^2 \left[2\tau G_M^2 + \frac{\cot^2\frac{\theta_e}{2}}{1+\tau}\left(G_E^2 + \tau G_M^2\right)\right] \tag{1.20}$$

which when substituted into the cross section formula (1.14), yields the Rosenbluth cross section as

$$\frac{d\sigma}{d\Omega_e} = \frac{\alpha^2}{Q^2}\left(\frac{E'_e}{E_e}\right)^2\left[2\tau G_M^2 + \frac{\cot^2\frac{\theta_e}{2}}{1+\tau}\left(G_E^2 + \tau G_M^2\right)\right]. \tag{1.21}$$

1.1.4 Rosenbluth Separation Technique

The Rosenbluth Separation Technique was used extensively starting in the 1970's to measure the Sachs form factors of the proton. It involves using the reduced cross section defined to be

$$\left(\frac{d\sigma}{d\Omega}\right)_{reduced} = \epsilon(1+\tau)\frac{\left(\frac{d\sigma}{d\Omega_e}\right)_{exp}}{\left(\frac{d\sigma}{d\Omega}\right)_{Mott}} = G_M^2 + \frac{\epsilon}{\tau}G_E^2 \tag{1.22}$$

where ϵ symbolizes the longitudinal polarization of the virtual photon. If the Q^2 value of the reaction is held constant, the virtual photon polarization may be varied by changing the beam energy and the scattering angle of the electron. If the elastic *ep* cross sections at a constant Q^2 is measured for different virtual photon polarizations, the Sachs form factors can be extracted by linearly fitting a plot of the reduce cross section against the value ϵ. The slope of the resulting fit is equal to $\frac{1}{\tau}G_E^2$ while its intercept is equal to G_M^2. The method is demonstrated on Figure 1.2 for the Q^2 values of 2.5, 5.0 and 7.0 GeV^2 using data from [14]. The 2.5 GeV^2 data is shown as open triangles, the 5.0 GeV^2 data as open circles and the 7.0 GeV^2 as closed triangles.

Even though the technique was very effective in measuring the Sachs form factors at low Q^2, the same cannot be said for high Q^2. First, the kinematic factor, τ, is proportional to Q^2 resulting in a dominance of the magnetic term in the reduce cross

Figure 1.2: The Rosenbluth separation technique demonstrated using data from [14]. A plot of the reduced cross section against the polarization of the photon, for several points taken at constant Q^2, is linearly fit. The resulting slope of the fit yields the value of τG_M^2 while its intersection is equal to G_E^2. The figure is from [11].

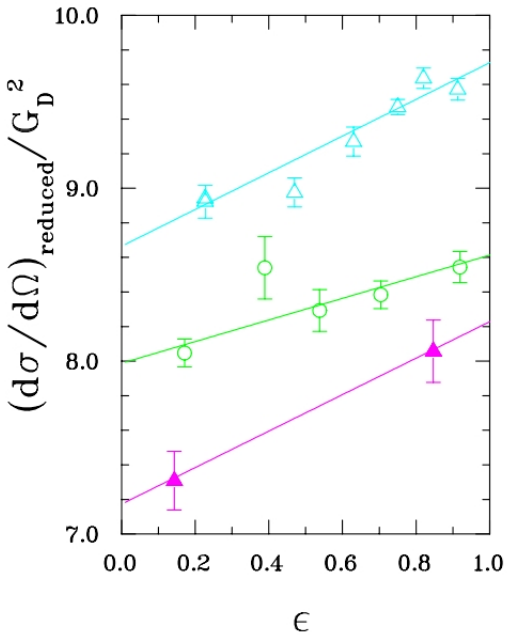

section at higher Q^2. Furthermore, the normalization of G_E^p differs from G_M^p by a factor equal to the magnetic moment of the proton. As a result, G_M^p will contribute to the reduced cross section by a factor of μ_p^2 greater than G_E^p.

1.1.5 Recoil Polarization Technique

At high Q^2 values, the Recoil Polarization Technique (RPT) has been found to be very effective in extracting the Sachs form factors. If the recoil proton is polarized, it implies that the polarization is preferentially in one direction over the other. In turn, the hadronic tensor is modified by the addition of a polarized hadronic tensor.

Furthermore, the RPT requires a longitudinally polarized electron beam, resulting in the modification of the leptonic tensor. As a result, the calculation of the modified amplitude gives rise to a longitudinal component (parallel to the proton momentum) of the polarization of the proton of the form

$$hP_l = h\frac{E_e + E'_e}{m_p I_0}\sqrt{\tau(1+\tau)}(G_M^p)^2 \tan^2\frac{\theta_e}{2} \tag{1.23}$$

and a transverse component in the scattering plane of the form

$$hP_t = -h\frac{2}{I_0}\sqrt{\tau(1+\tau)}G_E^p G_M^p \tan\frac{\theta_e}{2}. \tag{1.24}$$

Here, h is the polarization of the proton beam and $I_0 = G_E^{p2} + \frac{\tau}{\epsilon}G_M^2$. If the two components are measured simultaneously, the form factor ratio can be extracted as

$$\frac{G_E^p}{G_M^p} = -\frac{E_e + E'_e}{2m_p}\frac{hP_t}{hP_l}\tan\frac{\theta_e}{2}. \tag{1.25}$$

The recoil polarization technique has several advantages over the Rosenbluth Separation technique. For one, only a single measurement per Q^2 is required to extract the ratio. Furthermore, by measuring the interference term $G_E^p G_M^p$, the electric form factor can be measured with a higher accuracy. Finally, since the ratio is proportional to the ratio of the polarization components, knowledge of the electron beam helicity and the analyzing power of the polarimeter are not required. As will be explained in the next section, however, precision measurement of the analyzing power is still highly desirable in order to reduce the error in the form factor measurement.

1.2 Analyzing Power Problem

A beam of charged particles of momentum $\vec{k}$ incident on a target will scatter with a distribution that depends on the polar angle θ with respect to $\vec{k}$. If the incident beam also has spin, then there will also be a dependence on the azimuthal angle ϕ measured in the plane perpendicular to $\vec{k}$ as illustrated in Figure 1.3. There exist an

Figure 1.3: An incident polarized beam of particles of momentum $\vec{k}$ incident on a target will have a distribution depending on the polar and azimuthal scattering angles. The azimuthal scattering angle is measured in the plane perpendicular to the incident particle momentum.

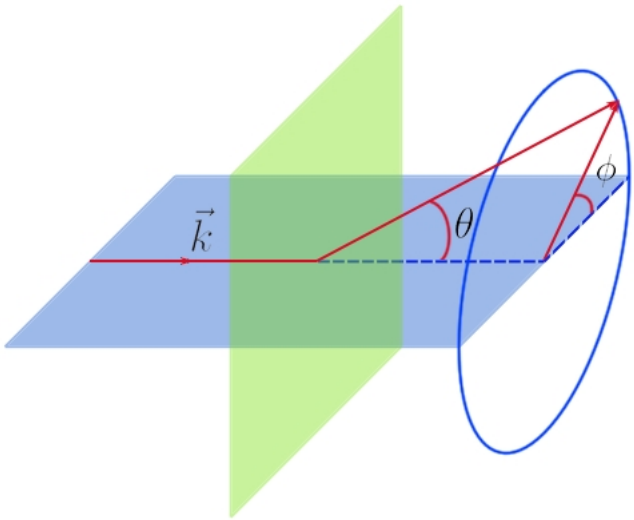

azimuthal scattering angle dependence on the polarization of a beam incident on an unpolarized target of spin j due to a spin-orbit coupling term of the form

$$V_{so} = U_{so}(r)\vec{L} \cdot \vec{S}$$

in the strong potential. Here, $\vec{L}$ is the orbital angular momentum of the charged particles with respect to the target nucleus, and $\vec{S}$ is its spin angular momentum.

Taking the gradient reveals the effect of such a potential on the force experienced by the charged particles

$$\begin{aligned} \vec{F}_{so} &= -\vec{\nabla}\left(U_{so}(r)\vec{L}\cdot\vec{S}\right) \\ &= -\frac{\partial U_{so}}{\partial r}\left(\vec{L}\cdot\vec{S}\right)\hat{r} - U_{so}(r)\vec{\nabla}\left(\vec{L}\cdot\vec{S}\right). \end{aligned} \tag{1.26}$$

Without working out the details of the second term of (1.26), the first term reveals that the radial force is proportional to the scalar product between $\vec{L}$ and $\vec{S}$. From Figure 1.4 and equation (1.26), it follows that a charged particle in a spin up state will scatter to the left of the target or analyzer nucleus while a charged particle in a spin down state will scatter to the right. An observation of an asymmetry in the azimuthal scattering angle will imply that the charged beam has more particles in a spin-up state than in a spin-down state (or vise versa), indicating the beam is polarized.

Quantitative measurement of this dependence is defined to be the analyzing power of the reaction. The analyzing power can be extracted directly by measuring the asymmetry in the azimuthal scattering angle of the beam within the target or analyzer. If the number of particles scattered at an angle ϕ and θ is counted to be $N_L(\theta,\phi)$ while those scattered at an angle $\phi+\pi$ and θ is found to be $N_R(\theta,\phi+\pi)$, then the scattering asymmetry is defined to be

$$A(\theta,\phi) = \frac{N_L - N_R}{N_L + N_R}. \tag{1.27}$$

Equation (1.27) can also be expressed in terms of the differential cross sections for

Figure 1.4: When a polarized beam scatters from an unpolarized target, an asymmetry will be observed due to the spin-orbit coupling term in the strong potential. A charged particle in a spin up (spin down) state will scatter to the left (right) of the target or analyzer nucleus.

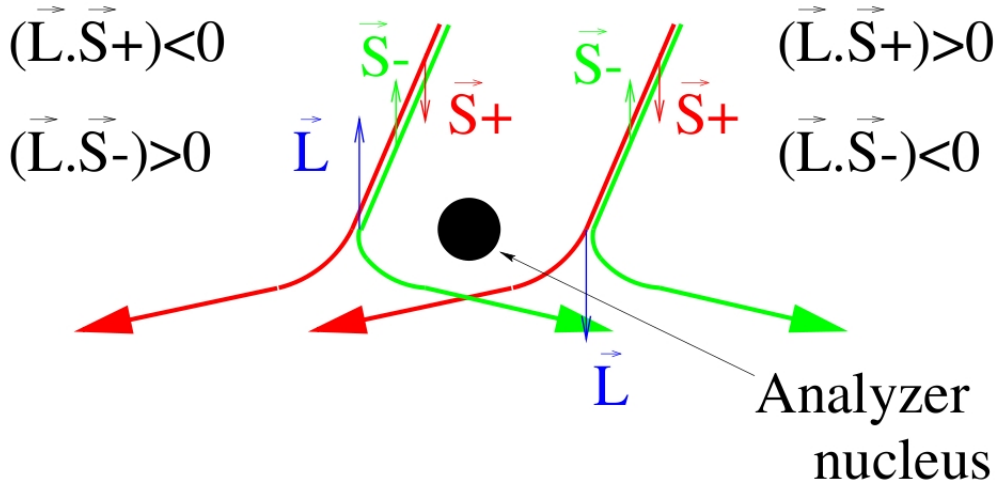

scattering to the left, σ_L and right, σ_R, as

$$A = \frac{\sigma_L - \sigma_R}{\sigma_L + \sigma_R}. \tag{1.28}$$

The differential cross section for a parity conserving spin 1/2 particle of initial momentum $\vec{k}$ and final momentum $\vec{k}_f$ scattering on a target of spin j was derived by Sachs in [15] to be

$$\sigma = \sigma_0 + (2 \text{ Re } a_1(k, \ \cos\theta) - b_1(k, \ \cos\theta)) \left(\hat{n} \cdot \vec{P}_i\right). \tag{1.29}$$

Here, a_1 may be a complex function of the particle momentum, k and the cosine of the polar scattering angle, θ, and b_1 is a real function of k and $\cos\theta$. Furthermore, $\vec{P}$

is the beam polarization, σ_0 is the differential cross section of an unpolarized beam and $\hat{n}$ is a unit vector normal to the scattering plane

$$\hat{n} = \frac{k \times k_f}{|k \times k_f|}.$$

Since the cross sections of particles scattering to the left and those scattering to the right differ only by the direction of the unit vector, $\hat{n}$, equation (1.29) can be used to recast equation (1.28) as

$$\begin{aligned} A &= \frac{\sigma_0 + (2\ \mathrm{Re}\ a_1 - b_1)\left(\hat{n}\cdot\vec{P}_i\right) - \sigma_0 + (2\ \mathrm{Re}\ a_1 - b_1)\left(\hat{n}\cdot\vec{P}_i\right)}{\sigma_0 + (2\ \mathrm{Re}\ a_1 - b_1)\left(\hat{n}\cdot\vec{P}_i\right) + \sigma_0 - (2\ \mathrm{Re}\ a_1 - b_1)\left(\hat{n}\cdot\vec{P}_i\right)} && (1.30) \\ &= \frac{2\,(2\ \mathrm{Re}\ a_1 - b_1)\left(\hat{n}\cdot\vec{P}_i\right)}{2\sigma_0} && (1.31) \\ &= A_y(\hat{n}\cdot\vec{P}_i) && (1.32) \end{aligned}$$

where the analyzing power has been defined as

$$A_y = \frac{(2\mathrm{Re}\ a_1 - b_1)}{\sigma_0}. \tag{1.33}$$

Using the analyzing power definition from (1.33), the total differential cross section can be rewritten as

$$\sigma = \sigma_0\left[1 + A_y\left(\hat{n}\cdot\vec{P}_i\right)\right]. \tag{1.34}$$

This gives an insight into the nature of the analyzing power and its relation to the strong interaction. A simple interpretation, however, is that the analyzing power describes the strength of the spin-orbit interaction.

The significance of the measurement of the analyzing power by the G_E^p-III collaboration is twofold. The first lies in its importance in optimizing the design of polarimeters to be used in future experiments. Precise knowledge of the analyzing power allows for the optimization of the analyzer for the range of momenta which the experiment will study resulting in a reduction in systematic error associated with the polarimeter.

Measurement of the analyzing power with as high a precision as possible is also desirable in order to decrease the error in the polarization observables. The error in the measurement of the polarization observables is defined to be [16]

$$\Delta(A_y P_t^{fpp}) = \Delta(A_y P_n^{fpp}) = \sqrt{\frac{2}{N_0 \mathrm{COM}}} \tag{1.35}$$

where COM is the coefficient of merit. The COM describes the efficiency of the instrumentation used to measure the polarization of the proton beam and is directly proportional to the square of the analyzing power as

$$\mathrm{COM} = \int_{\theta_{min}}^{\theta_{max}} \varepsilon(\theta) A_y^2(\theta) d\theta \tag{1.36}$$

where ε is the efficiency of the polarimeter defined as

$$\varepsilon = \frac{N_{eff}(\theta)}{N_0}.$$

Here, N_{eff} is the number of protons which pass the analysis cuts and scatter at a polar angle θ and N_0 is the total number of protons incident on the polarimeters which pass the elastic cuts. As follows from equations (1.35, 1.36), an increase in the

analyzing power leads to a significant decrease in the error of polarization observables. Since the uncertainty in the measurement of the form factor ratio is a result of the propagation of the uncertainty in the measurement of the polarization observables, precision measurement of the analyzing power will greatly influence the final result.

1.3 Previous Measurements

1.3.1 $\mu_p G_E^p/G_M^p$ Measurements

Figure 1.5: A compilation of measurements of G_E^p and G_M^p normalized to the dipole form factor made by [14], [17], [18], [19], [20], [21], [22], [23], [24], [25], [26], [27], [28], [29] and [30] using the Rosenbluth Separation Technique. The figure is taken from [11].

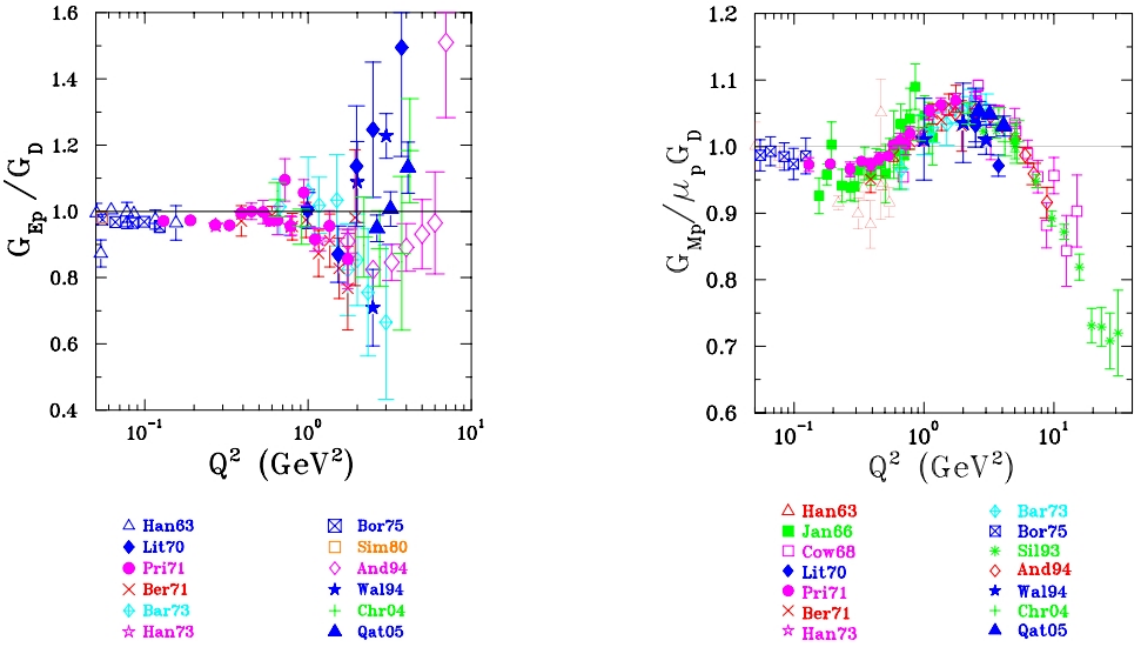

The earliest measurements of the Sachs form factors by [14, 17, 18, 19, 20, 21, 22, 23, 24, 25, 26, 27, 28, 29, 30] using the Rosenbluth Separation Technique found the

electric and magnetic form factors to be well described at low Q^2 by the empirical formula

$$G_E^p = \left(1 + \frac{Q^2}{.71\text{GeV}^2}\right)^{-2} = G_D$$

$$G_M^p = \mu_p G_D$$

where G_D is the dipole form factor. A compilation of the data is shown on Figure 1.5. The difficulty in measuring G_E^p using the Rosenbluth Separation technique is apparent in its large errors above $Q^2 \approx 2$ GeV^2. In contrast, G_M^p is well behaved even at $Q^2 = 30$ GeV^2 which implies its dominant nature over G_E^p in the reduce cross section.

Measurements of G_E^p/G_M^p made by [31, 32, 33, 34, 35, 36, 37, 38, 39, 40] using the Recoil Polarization Technique are compare with those made using the Rosenbluth Separation Technique (in green) on Figure 1.6. The data obtained using the recoil polarization technique seem to clearly indicate that G_E^p is decreasing at a much faster rate than G_M^p with increasing Q^2. This is unlike the conclusion that can be reached using the Rosenbluth separation data which expresses the opposite effect. It is thought that the discrepancy in the Rosenbluth separation method can be explained by taking into account the effects of two photon exchange on the Rosenbluth cross section. The two gamma experiment (E04-019) which ran concurrently with the G_E^p-III experiment is set to measure this contribution using three different photon polarizations at $Q^2 =$ 2.5 GeV^2.

1.3.2 Analyzing Power Measurements

The most recent measurements of the analyzing power for the reaction $\vec{p}$+CH_2 were conducted at the JINR-VBLHE (Dubna) accelerator complex at four different

Figure 1.6: A compilation of the measurements of G_E^P/G_M^p made by [31], [32], [33], [34], [35], [36], [37], [38], [39], and [40] using the Recoil Polarization Technique compared to those made using the Rosenbluth Separation Technique (highlighted in green). The measurements in blue were made by the G_E^p-I collaboration while those in red where made by the G_E^p-II collaboration. The figure was taken from [11].

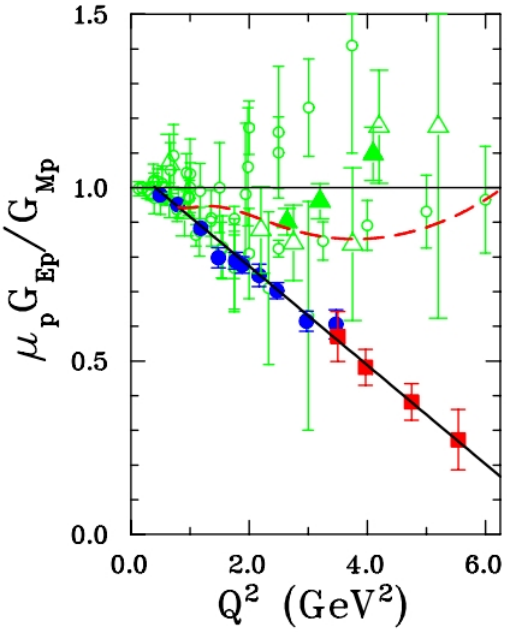

proton momentums: 1.75, 3.8, 4.5 and 5.3 GeV/c [41]. The polarized protons incident on the CH_2 were produced by fragmentation of a vector polarized beam of deuterons from a Be target. The polarization of deuteron beam was measured by a pair of polarimeters located at the exit of the POLARIS ion source and after the extraction point of beam. The polarization of the proton beam was extracted by looking at the asymmetry in the azimuthal scattering angle as measured by the POMME polarimeter. The analyzing power measurements as a function of the transverse momentum, p_t are shown on Figure 1.7.

Figure 1.7: Analyzing powers for the reaction $p + CH_2 \rightarrow X$ measured at proton momenta 1.75, 3.8, 4.5, and 5.3 GeV/c. It follows from the figure that the analyzing power decreases with increasing proton transverse momentum.

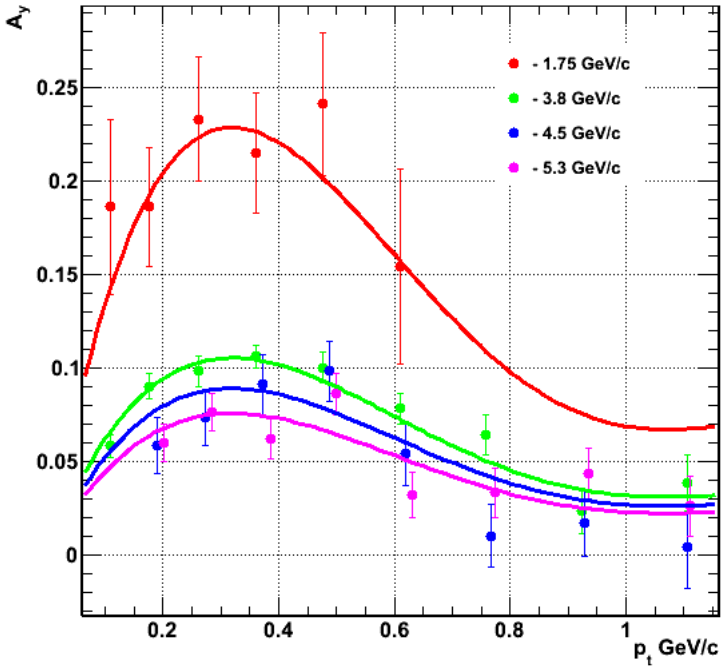

It is generally observed that the analyzing power decreases with increasing proton momentum. The Dubna collaboration was able to parametrize this behavior by a fourth order polynomial as follows

$$A_y(p_t, p_{lab}) = \frac{\sum_{i=1}^{4} c_i p_t^i}{p_{lab}} \tag{1.37}$$

where p_t is the transverse momentum, p_{lab} is the proton momentum and c_i are constants listed on Table 1.2 . The transverse momentum pt is a convenient parameter

Table 1.2: Fitting parameters with errors for the Dubna parametrization of the analyzing powers.

c_1	c_2	c_3	c_4
3.02 ± 0.13	-7.33 ± 0.66	6.17 ± 1.11	-1.74 ± 0.59

for displaying the analyzing power for several different proton momenta in the same graph.

The effect of the analyzer thickness on the analyzing power was also studied and

Figure 1.8: Analyzing powers measured using the target thicknesses of 37.5, 51.6, 65.7 and 79.8 g/cm^2 at a proton momentum of 3.8 GeV/c. It was found that the analyzing power for the reaction $p + CH_2$ was independent of the analyzer thickness.

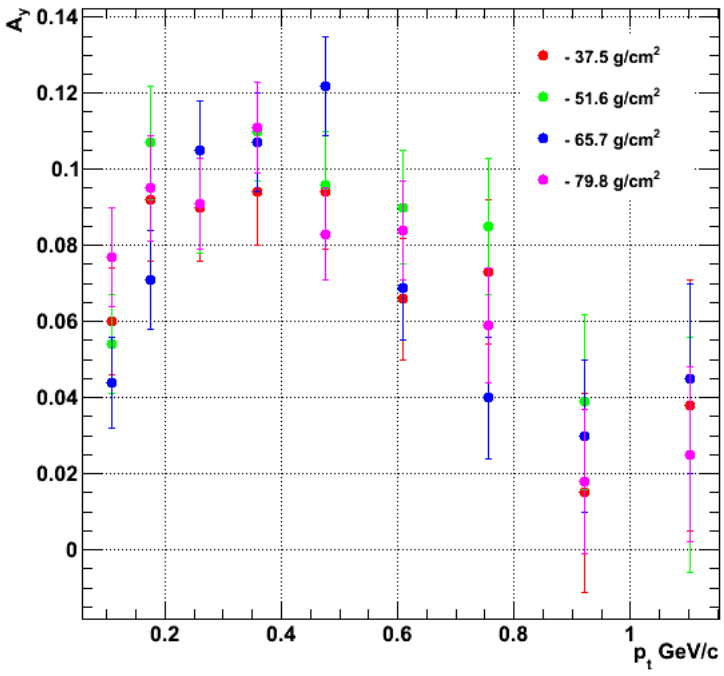

the results are shown on Figure 1.8. Analyzing power measurements using a 3.8 GeV/c proton beam were taken using four analyzer thicknesses: 37.5, 51.6, 65.7 and 79.8 g/cm^2. It was concluded that, within the statistical uncertainty, the analyzing power at $p_{lab} = 3.8$ GeV/c was independent of the analyzer thickness.

Analyzing power measurements for the reaction p+$CH_2 \rightarrow X$ were also made by the G_E^p-II (E99-007) [33] collaboration at JLab using the recoil polarization tech-

Figure 1.9: Analyzing power measurements made by the G_E^p-II collaboration at proton momenta 1.8, 2.1, 2.5 and 3.0 GeV plotted against the polar angle. The figure is taken from [16].

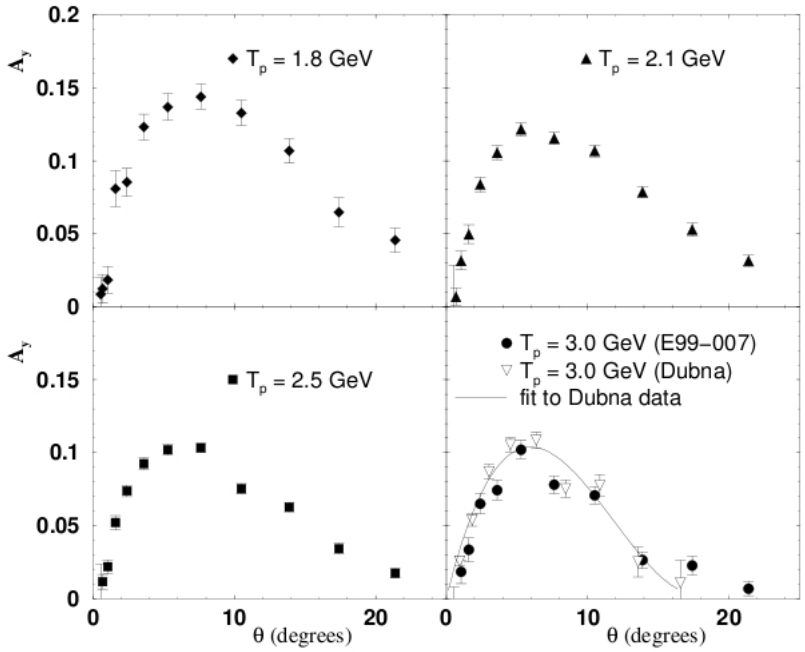

nique. A polarized electron beam was elastically scattered from a liquid hydrogen target producing an electron and polarized proton in the final state. By measuring the asymmetry in the azimuthal scattering angle of the protons incident on a fo-

cal plane polarimeter, the polarization of the proton beam was extracted. In turn, this allowed for the extraction of G_E^p/G_M^p and the analyzing powers. The analyzing power measurements made for protons of incident momenta 1.8, 2.1, 2.5 and 3.0 GeV are shown as a function of polar scattering angle on Figure 1.9. The measurements made by the G_E^p-II collaboration were done using similar methods to those used by the G_E^p-III collaboration and, thus, serve as a good primer for comparison to the measurements made here.

Chapter 2

G_E^p Experimental Apparatuses

The G_E^p-III experiment was conducted at the Thomas Jefferson National Accelerator Facility (TJNAF) in Newport News, Virginia within Experimental Hall C. The experiment took place during the period of October 2007 to June 2008 and saw a total of seven kinematic settings. The kinematic settings are listed on Table 2.1.

Table 2.1: The seven kinematic settings at which the G_E^p-III experiment took data. The table lists the energy of the electron beam, the four momentum transfer squared, the recoil proton momentum, the energy of the scattered electron, the proton and electron scattering angles and the BigCal distance from the target.

E_{beam} [GeV]	Q^2 [GeV^2]	p_p [GeV/c]	E_e [GeV/c]	θ_p [^{o}]	θ_e [^{o}]	r [m]
2.528	2.733	2.2032	1.072	24.990	60.3	9.60
4.045	5.200	3.5887	1.274	17.960	60.3	6.05
1.867	2.500	2.0676	0.535	14.495	104.6	4.75
2.839	2.500	2.0676	1.507	30.985	44.9	12.00
3.539	2.500	2.0676	2.207	35.395	32.9	11.15
5.714	6.800	4.4644	2.090	19.098	44.3	6.00
5.714	8.538	5.4073	1.164	11.595	69.0	4.30

The Continuous Electron Beam Accelerator Facility (CEBAF) simultaneously provided polarized electrons with energies upwards of 5.714 GeV to each of three experimental halls as depicted on Figure 2.1. The polarized electrons delivered to Hall C elastically scattered from a liquid hydrogen target (LH_2). The polarized proton and scattered electron beams were then detected, in coincidence, by the High Momentum Spectrometer (HMS) and an electromagnetic lead glass calorimeter (BigCal), respectively. Coincidence detection resulted in a significant reduction of inelastic events

which would otherwise mask the elastic peak. The proton polarization was measured using a Focal Plane Polarimeter (FPP). The FPP consist of two blocks of CH_2 with pairs of drift chambers interleaved. This is followed by a smaller lead glass calorimeter (HMSCal) which will be used to discriminate between protons and neutrons emerging from the CH_2 analyzers. In the chapter that follows, a detailed description of each experimental apparatus will be given.

2.1 Continuous Electron Beam Accelerator Facility

Figure 2.1: The Continuous Electron Beam Accelerator Facility provides a polarized electron beam of energies upwards to 5.714 GeV simultaneously to three experimental halls.

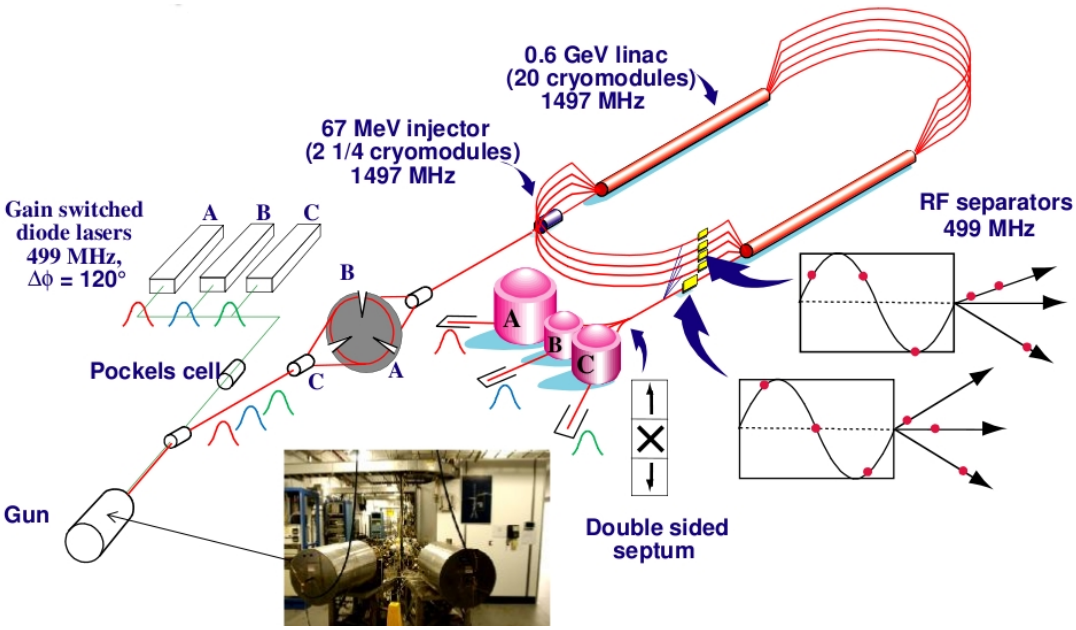

2.1.1 Electron Production and Injection

The polarized electrons injected into the accelerator were a result of photoemission

from a superlattice photocathode. The superlattice cathode structure of the photocathode consisted of a 5 nm layer of Gallium Arsenide (GaAs) followed by 14 layers of 4 nm GaAs Phosphide with 3 nm layers of GaAs interleaved. The 14 pairs of layers as well as the 5 nm coat were doped with Beryllium to a concentration of 5×10^{17} cm^{-3} and 5×10^{19} cm^{-3}, respectively. The addition of the different layers to the photocathode lowers its vacuum level below its conduction band allowing electrons to be emitted. The use of the superlattice cathodes has allowed the polarization of the electron beam to reach approximately 85% with a Quantum Efficiency (QE) of $\approx 1\%$. Additional details regarding the photocathode may be found in [42].

Each of the three experimental halls has a dedicated gain-switched fiber coupled laser of wavelength 1560 nm. The lasers are frequency doubled in order to produce light of wavelength of 790 nm, matching the band gap of the superlattice cathode. The lasers are phased shifted by 120^o and are each pulsed for ≈ 40 ps at 499 MHz [43]. The combined frequency of the electron bunches is 1497 MHz which matches the operational frequency of the accelerator cryomodules. Polarization of the photoemission electrons is achieved by circularly polarizing the light incident on the photocathode using Pockel cells. The light can be polarized either to the left or the right with each direction corresponding to a different helicity state. The Pockel cells switch the polarization of the light at a steady rate in order to allow data acquisition for both helicity states of the electron beam.

The photoemission electrons are released into an extremely high vacuum environment at a pressure of 10^{-11} to 10^{-12} Torr. This level of vacuum is required in order to reduce the number of ions which backscatter onto the cathode, resulting in an increase of the lifetime and QE of the superlattice cathode. The free electrons are

then delivered into the injector by a 100 keV electron gun. The injector itself then accelerates the electron bunches to an energy of 67 MeV by 2 1/4 cryomodules before being delivered into the accelerator. A description of the cryomodules will be given in the next section.

2.1.2 Electron Acceleration

The CEBAF accelerator is composed of two linacs arranged in a racetrack configuration as shown on Figure 2.1. Each of the linacs consist of 20 cryomudules which is capable of accelerating the electron bunches by 0.57 GeV per pass up to a maximum of 5 passes per linac. The number of passes depends on the energy requirements of the experiments taking place. The electron bunches are then delivered to each experimental hall by an RF separator operating at a frequency of 499 MHz.

Figure 2.2: A 5-cell ultra-pure Niobium superconducting radio frequency (SRF) cavity used to accelerate electrons at CEBAF. Each of the accelerator linacs contains 160 SRF cavities operating at a frequency of 1497 MHz.

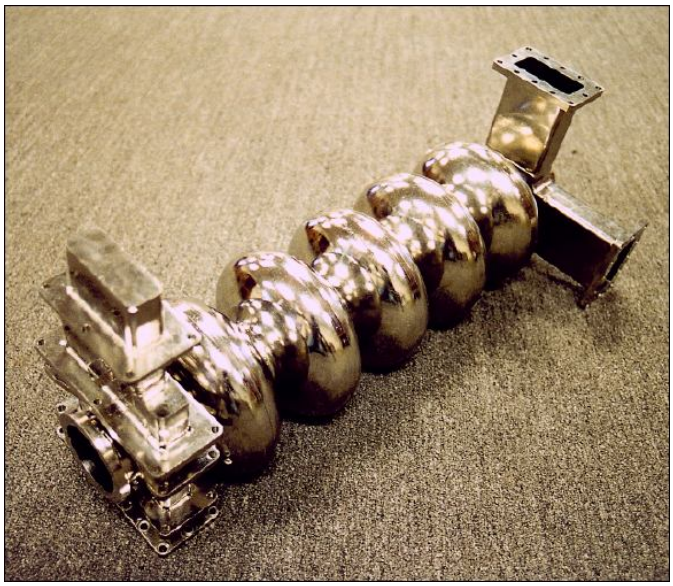

The acceleration of the electron beam takes place using 5-cell superconducting radio frequency (SRF) cavities made of ultra-pure Niobium operating at 1497 MHz. A picture of one of the 5-cell SRF cavities used by CEBAF is shown on Figure 2.2. Two of the SRF cavities are joined and placed in a sealed helium container forming a cryounit. Four cryounits are then joined in an insulating vacuum environment to form a cryomodule. The cryomodules also contain the necessary instrumentation both to power the SRF cavities and keep them at an operating temperature of 2 K [44].

2.1.3 Beam Energy Measurement

The energy of the electron beam was obtained in either of two ways: either through calculation using two body kinematics or through the arc measurement using the Hall C transport line. The transport line consist of 8 dipoles, 12 quadrupoles, 8 sextupoles and 8 beam correctors. However, during the arc measurements of the beam energy all but the dipoles are turned off.

An electron beam which enters the arc is bent by a total of 34.3^o from its initial trajectory by the dipoles.The initial and final beam positions are measured by pairs of wire scanners (superharps) located at the entrance and exit of the transport line. A third superharp, placed midway the transport line, measured the electron beam curvature. The momentum of the beam is then determined as

$$p = \frac{e}{\theta_{beam}} \int \vec{B} \cdot d\vec{l}. \tag{2.1}$$

where e is the electron charge, θ_{beam} is the measured curvature of the beam and B is the magnetic field of the dipoles.[7] Using this method, the beam momentum can be

[7]It must be noted that the magnetic field of the dipoles is mapped as a function of current using a standalone dipole. The field map is then used to calibrate the transport line dipoles.

obtain with an accuracy of 5×10^{-4}. A more detailed description of the arc energy method can be found here [45].

Figure 2.3: Beam energy calculated using 2-body kinematics. The peak was fit with a Crystal Ball function while the background was fit with a Gaussian.

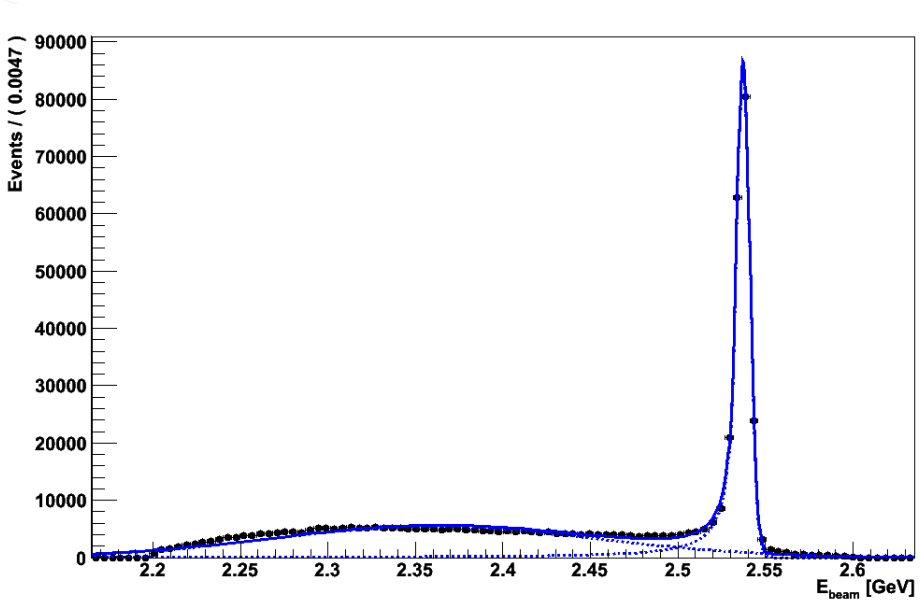

All Q^2 points except for $Q^2 = 2.733$ GeV^2 (kinematic 3) obtained a beam energy measurement using the arc method. The beam energy for kinematic 3 was obtained using strictly 2-body kinematics and is shown on Figure 2.3. The energy was fit using a Crystal Ball function to represent the signal portion of the graph while the background was fit to a Gaussian. A description of the Crystal Ball function and its parameters is given in Appendix B. From the fit results shown on Table 2.2, the signal resolution and accuracy were found to be $\frac{\sigma_E}{E} \approx .15\%$ and $\approx 10^{-3}$, respectively, which is comparable to the resolution and accuracy of the arc method.

Table 2.2: The results of the fit to the beam energy. The signal resolution and accuracy were found to be $\frac{\sigma_E}{E} \approx 0.15\%$ and 10^{-3}, respectively.

	Crystal Ball (sig)	Gaussian (bkg)
$\bar{E}$ [GeV/c]	$2.537 \pm 1.057 \times 10^{-5}$	$2.361 \pm 2.375 \times 10^{-4}$
σ_E [GeV/c]	$3.916 \times 10^{-3} \pm 9.185 \times 10^{-6}$	$9.257 \times 10^{-3} \pm 1.774 \times 10^{-4}$
α	$1.256 \pm 5.598 \times 10^{-3}$	–
n	$1.501 \pm 1.531 \times 10^{-2}$	–

2.1.4 Møller Polarimeter

Measurement of the polarization of the electron beam delivered to Hall C, is crucial to the extraction of both the proton form factors and the analyzing power. The measurements were done using the Hall C Møller polarimeter depicted on Figure 2.4. As its name suggest, the Møller polarimeter makes use of Møller scattering ($\vec{e} + \vec{e} \rightarrow e + e$) whose production cross section in the center of mass (CM) is known from QED as [46]

$$\frac{d\sigma}{d\Omega} = \frac{d\sigma_0}{d\Omega} \left[1 + P_t^{||} P_b^{||} A_{zz}(\theta)\right].$$

Here $\frac{d\sigma_0}{d\Omega}$ is the unpolarized cross section, $P_t^{||}$ and $P_b^{||}$ are the polarization of the target and the beam, respectively, and A_{zz} is the analyzing power of the reaction[8].

The Møller polarimeter consist of a thin iron target oriented perpendicular to the electron beam. It is magnetized to saturation by a superconducting coil which produces a 4 Tesla field along the axis of the beam. This produces a polarized target whose polarization is known to an accuracy of $\frac{1}{4}\%$. By magnetizing the iron target, an asymmetry in the production cross section arises which can be used to determine

[8]For the explicit form of the unpolarized cross section and the analyzing power see [46].

Figure 2.4: The Hall C Møller Polarimeter used to measure the polarization of the beam delivered during the experiment.

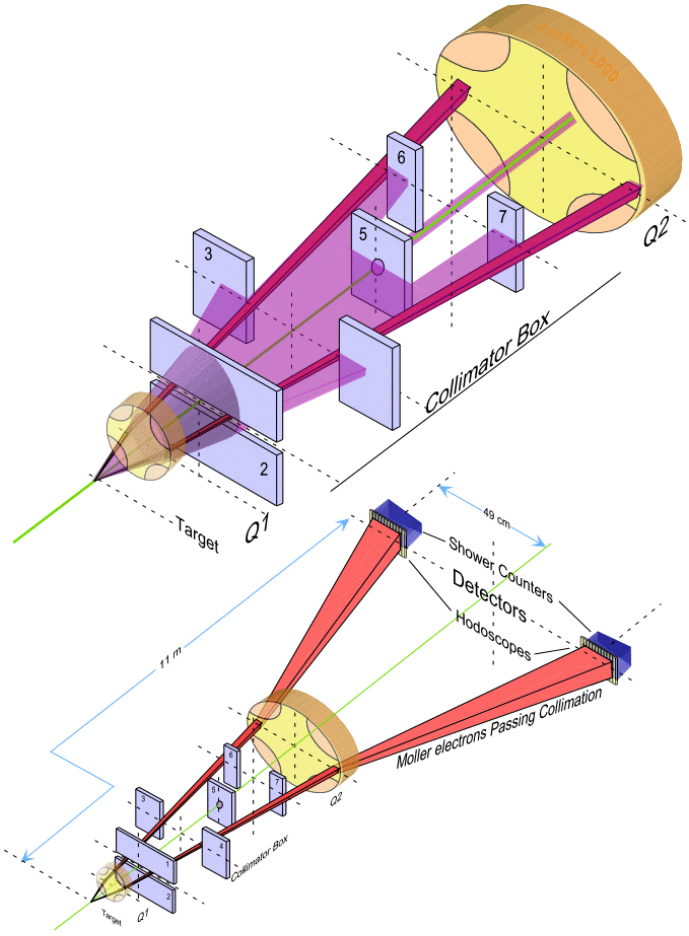

the polarization of the beam as

$$P_b^{||} = \frac{\left(d\sigma^{\uparrow\uparrow}/d\Omega\right) - \left(d\sigma^{\uparrow\downarrow}/d\Omega\right)}{\left(d\sigma^{\uparrow\uparrow}/d\Omega\right) + \left(d\sigma^{\uparrow\downarrow}/d\Omega\right)} \frac{1}{P_t^{||} A_{zz}}.$$

The exact form of the analyzing power is known from QED and was chosen such that the production cross section is maximized. This seems to occur at CM scattering

angles of 90^o which have a maximum analyzing power of -7/9. Use of this method allows the beam polarization to be measured with an accuracy of about 1/2% [46].

Several collimators were used select the desired scattering angles of electrons emerging from the iron target. This reduces the amount of background which comes mainly from Mott scattering. Quadrupoles were placed before and after the collimators in order to guide the scattered electrons away from the beam direction. This is done to allow the placement of shower counters to measure the rate of production of Møller electrons[9] without interfering with the beam line.

The problems which arose with the 5th pass RF separator during the run of kinematic 3 prevented any Møller measurement to be made. Instead, the average of all beam polarization measurements made during the G_E^p-III experiment was used in the extraction of the analyzing power. This amounts to a beam polarization of $\bar{P}_b = 82.68\%$.

2.2 Cryogenic Target

The target configuration used for the G_E^p-III experiment consisted of three cryogenic loops used for liquid hydrogen (LH_2) and solid targets consisting of aluminum, carbon, and copper. The sole use of the solid targets was to calibrate the HMS optics. All of the targets were mounted on a ladder system contained within an aluminum scattering chamber. The scattering chamber had thin aluminum exit windows on either side with large scattering angle acceptances to allow the scattered proton and electrons to escape freely. The scattering chamber was maintained at a pressure of 24 ± 1 psiA during the duration of the experiment.

[9]It is worth mentioning that the Hall C Møller polarimeter is unique in that the electrons are detected in coincidence by the shower counters leading to a further reduction in background.

During the running of kinematic 3, only the first loop which consisted of a 20 cm and a 4 cm LH_2 target was used. The LH_2 was constantly cycled through the loop by a 60 MHz fan and was kept at an operating temperature of $19 \pm .5$ K. All excess heat acquired by the target through its interaction with the beam was carried away by a liquid helium cooling system operating at 14 K. The beam was also rastered by a raster magnet system to a size of 2×2 mm^2 in order to prevent local heating of the target. In order to avoid large fluctuations in the LH_2 temperature which may arise from variations in the the beam current, a high power heater was used to compensate for small drops in the LH_2 temperature. The adjustments by the heater are automated, however, the power may be adjusted manually if it were to fail.

2.3 High Momentum Spectrometer

The superconducting focusing High Momentum Spectrometer served as the hadron arm during the experiment. Three superconducting iron quadrupoles were used to focus the recoil proton beam while a dipole was used to guide the beam at a 25^o angle into the HMS hut. The HMS hut contains the HMS detector package which consist of a pair of drift chambers, the Focal Plane Polarimeter [10], scintillating hodoscopes and a lead-glass calorimeter. It also housed the data acquisition electronics used by the Focal Plane Polarimeter. The configuration of the HMS magnets along with the HMS hut is shown on Figure 2.5.

The HMS Magnets as well and the HMS Hut both lie on a common carriage which is able to rotate around the target. This allowed the HMS central momentum to be matched to the expected momentum of the recoiling protons which was calculated

[10]The Focal Plane Polarimeter replaced a gas Cherenkov counter which had been used by previous experiments for particle identification.

Figure 2.5: The High Momentum Spectrometer consist of a QQQD magnet configuration and is used as the hadron arm in the G_E^p-III experiment.

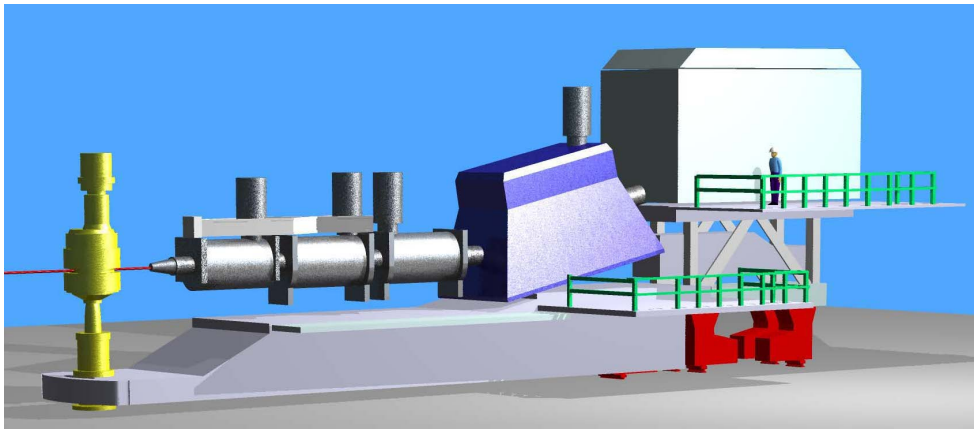

from *ep* 2-body kinematics. The HMS is capable of pivoting from 11.595^o to approximately 90^o degrees. This allows for the detection of particles with momenta ranging from 0.5 to 7.5 GeV/c. The angles at which the HMS was placed during the various kinematics of the G_p^E-III experiment are shown on Table 2.1. Some of the HMS performance properties are listed on Table 2.3 [47].

Table 2.3: The High Momentum Spectrometer performance properties.

HMS Performance Properties	
Maximum Central Momentum [GeV/c]	7.5
Momentum Bite $[(p_{max} - p_{min})/p_0]$ [%]	18
Momentum Resolution $\delta p/p$ [%]	<0.1%
Solid Angle Acceptance [msr]	>6
Useful Target Length [cm]	10
Vertex Reconstruction Accuracy [cm]	3.4

2.3.1 HMS Superconducting Magnets

The HMS quadrupoles are of superconducting cold-iron design[11] each designated as Q_1, Q_2, and Q_3. The quadrupoles Q_2 and Q_3 are identical in design while Q_1 has a more narrow width in order to allow the HMS to go to forward angles. Some of the properties of the quadrupoles are listed on Table 2.4[48].

Table 2.4: The properties of the High Momentum Spectrometer quadrupoles.

	Q_1	Q_2/Q_3
Gradient [G/cm]	605	405
"Good Field" Radius [cm]	22	30
Pole Tip Field [T]	1.5	1.56
Radius to Pole [cm]	25	35
Magnetic Length [cm]	189	210
Weight [tons]	20	30

The HMS dipole is positioned downstream from the three quadrupoles. It has approximate dimensions of $7.3 \times 3.9 \times 1.9\times$ m^3. It consist of two superconducting coils made of 0.8 cm diameter NbTi cable connected in series. Each coil consist of three double pancake coils. The dipole is cooled by liquid helium provided by a cryogenic system located outside of the dipole framework. Some of the properties of the dipole magnet are listed on Table 2.5 [49]

2.3.2 HMS Collimator

In order to define the angular acceptance of the HMS, an octagonal collimator, known as the pion collimator, was used. The collimator has a width of 9.150 cm and a height of 23.292 cm. It is made of 6.35 cm think Heavymet (90% W, 10% CuNi)

[11]The "cold-iron" quadrupole design was developed by Michigan State University and is unique in the sense that the field shaping is done primarily by iron poles. Cold-iron simply refers to the positioning of the iron yoke within the cryostat as opposed to warm iron design which has the iron yoke placed outside. A more detailed description of the design can be found in [48].

Table 2.5: The properties of the High Momentum Spectrometer dipole.

	Dipole
Gap [cm]	42
"Good Field" Width [cm]	± 30
Max. Pole Tip Field [T]	1.66 @ 6 GeV/c
Effective Length [m]	5.26
Coil Configuration	4.1×10^5 A-turns/pole
Operating Current	6,881 A
Weight [tons]	470

and is flared[12] in order to match the angular acceptance of the HMS. The collimator is mounted on a sliding rail located at a distance of 166.00 cm. A this distance from the target, a solid angle of 6.767 msr is subtended.

2.3.3 HMS Drift Chambers

Before continuing on to the details of the HMS drift chambers, some background on their operation is useful. The main purpose of a drift chamber is to measure the coordinates of a charge particle track traversing its volume. It typically consist of several planes of anodes (sense) wires with layers of cathode wires interleaved. The planes are oriented at different angles in order to allow for coordinate measurement in all three spatial dimensions. It is also common to place another set of wires (field wires) midway the sense wires in order to achieve as homogenous an electric field as possible.

All planes are enclosed within a volume filled with a gas mixture, such as argon/ethane, whose characteristic properties have been well studied. A charged particle traversing the drift chamber volume will ionize the gas atoms producing a trail

[12]The dimensions at its exit are larger than at the entrance.

of electrons along its path. By measuring the time it takes for the electrons to drift from their point of origin to the sense wires, the coordinate at the point of ionization can be determined as

$$x = \int_{t_0}^{t_1} u(t)dt \tag{2.2}$$

where u is the drift velocity as a function of time and t_0 and t_1 represent the start and end times of the electron drift. The start time of the electron drift is determined, after corrections for time of flight and signal propagation have been applied, using a scintillator placed upstream from the drift chambers. The end of the electron drift corresponds to the time when a signal is produced by one of the sense wires. A more detailed explanation of several drift chamber concepts can be found in [50].

The HMS detector package uses a pair of drift chambers located upstream from the Focal Plane Polarimeter to determine the initial trajectory of the proton track with a resolution of 115 μm per plane [51]. Each drift chamber volume consist of 6 planes of wires enclosed in an aluminum frame of dimensions $1.62 \times .78 \times .16$ m^3. The frame has a thin aluminized Mylar window on either side with an active area of 110×50 cm^2. Each plane of wires consist of 25 μm gold-plated tungsten sense wires surrounded by 150 μm gold-plated copper-beryllium field wires. The field wires are used to achieve a homogeneous electric field around the sense wire region minimizing any large variations in the electron drift velocity. The resulting drift cell measures 10×8 mm^2. The sense wires were held at ground-potential while the field wires were held at a negative potential provided by CAEN high voltage crates.

The first and last planes, X and X$'$, are at 0^o degrees as defined on Figure 2.6 with the second and fifth layers, Y and Y$'$, oriented orthogonal to them. The third and fourth layers, U and V, are tilted at 15^o measured from the horizontal as defined

Figure 2.6: The layer definitions of the High Momentum Spectrometer drift chambers. The X, X' planes lie orthogonal to the Y, Y' planes while the U and V planes are oriented at -15^o and 15^o, respectively.

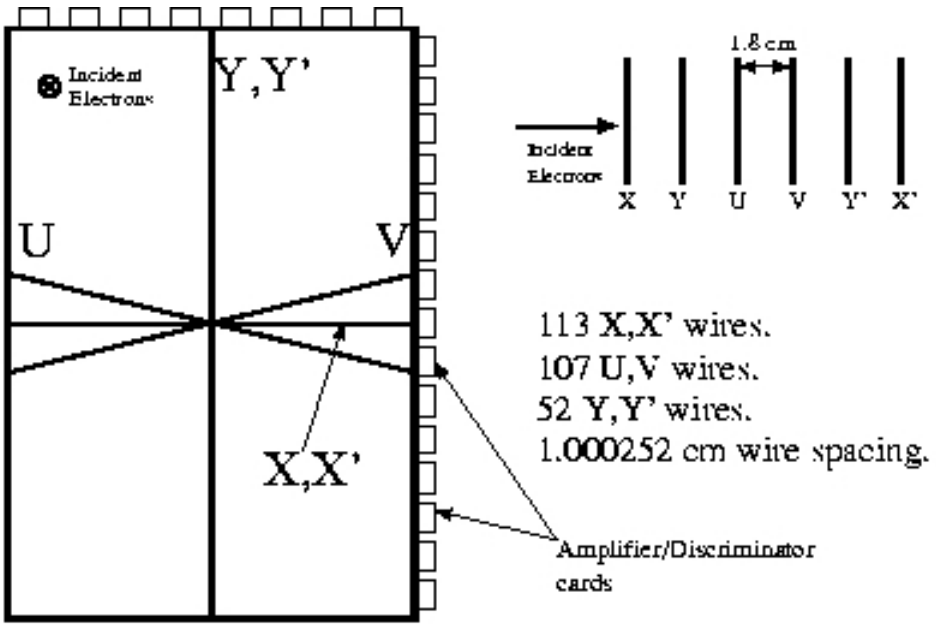

by the X and X′ planes. All planes are spaced 1.8 cm from each other.

The drift chamber volumes were filled with a 50:50 gas mixture of argon-ethane supplied by a source outside of Hall C. The properties of the mixture have been thoroughly studied and are well understood making it ideal to be used in the drift chambers. A more detailed description of the gas mixture properties is given in [52]. Before entering the drift chambers, the gas is passed through a bubbler filled with isopropyl alcohol maintained at 0^o C. As a result, the gas mixture was doped with approximately 1% alcohol. This is done in order to preserve the lifetime of the drift chambers even through experiments that see a high amount of event rates [53].

The exhaust gas was bubbled through mineral oil in order to maintain a fixed drift chamber pressure.

The signals from the sense wires were read out using Nanometrics N-277-L and Lecroy 2735DC amplifier-discriminator cards. Each of the cards was connected to 16 wires at a time and had their threshold voltage held at -5.5 V. These cards were then connected to Lecroy 1877 fastbus Time-to-Digital converters which were mounted inside of a fastbus crate located inside the HMS hut. For a more detailed description of the HMS drift chambers, see [51] and the references within.

2.4 Focal Plane Polarimeter

The primary function of the Focal Plane Polarimeter was to measure the asymmetry in the azimuthal scattering angles for the reaction $p + CH_2 \rightarrow X$. This was accomplished by reconstructing the tracks which emerged from the CH_2 (ana1 and ana2) by a pair of drift chambers (fpp1 and fpp2) located upstream from each analyzer. The electron drift start times were determined from the times the incident protons triggered a pair of scintillators (s1x and s1y) located downstream from the analyzers. The scattering angles were reconstructed by comparing the incident proton track, reconstructed by the HMS drift chambers (dc1 and dc2), to the each of the tracks reconstructed by fpp1 and fpp2. The configuration of the FPP components is shown on Figure 2.7.

2.4.1 FPP Drift Chambers

The FPP drift chamber volumes contained three detection planes oriented along -45^o, 0^o, and +45^o with respect to x-axis as shown on Figure 2.8. The planes were housed in an airtight aluminum volume of dimensions $1.91 \times 1.59 \times .112$ m^3. Either

Figure 2.7: The configuration of the FPP components. The FPP was composed of two blocks of CH_2 with pairs of drift chambers interleaved. It was used to measure the asymmetry in the scattering angles of the protons emerging from the CH_2 analyzers.

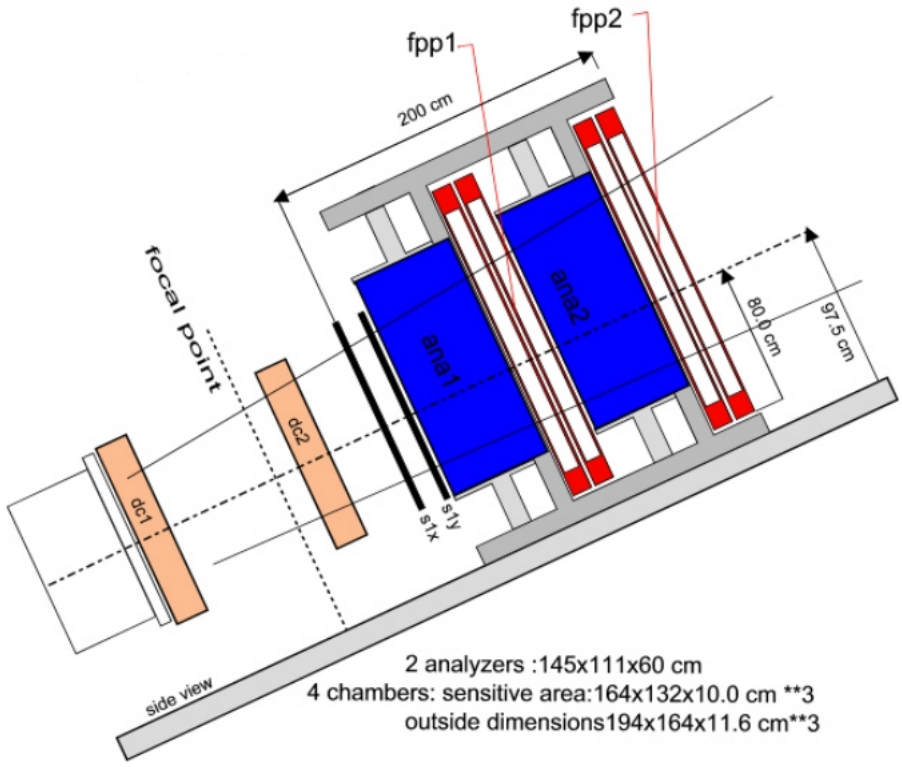

side of the volume contained a 30 μm thick window made of aluminized Mylar of active area 1.66×1.34 m^2. Each of the detection layers were separated by 1.6 cm with layers of cathode wires interleaved. Each detection plane contained a layer of sense wires spaced every 2 cm with field wires placed in between. The resulting drift cell measured 2.0 cm by 1.6 cm. Some of the properties of the wires used for each of the layers are listed on Table 2.6.

The $\pm 45^o$ planes each contained a total of 144 sense wires, while the 0^o plane con-

Figure 2.8: Orientation of the FPP drift wires. Each FPP drift chamber contains three planes of wires oriented at $\pm 45^o$ and 0^o.

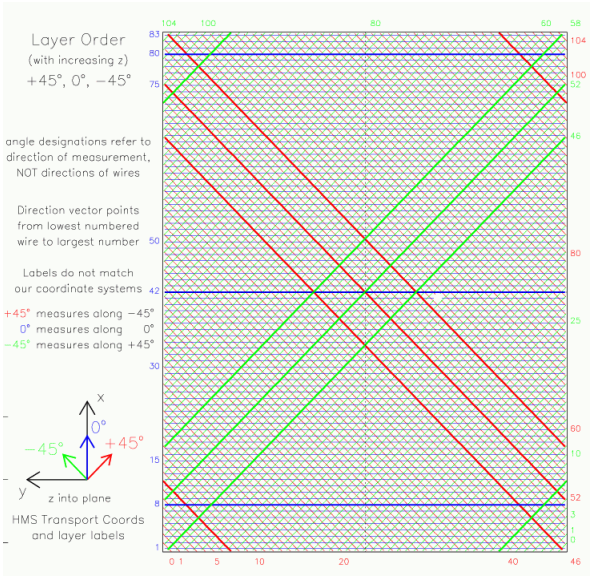

Table 2.6: Some of the properties of the wires used by the FPP drift chambers.

	material	diameter [cm]	tension [g]	potential [V]
sense wires	Au plated W	30 μm	70	0
field wires	Be + Bronze alloy	100 μm	150	2,750
cathode wires	Be + Bronze alloy	80 μm	120	2,350

tained 83. All of the wires were connected in bundles of 8 to discriminating/amplifying cards. The discriminating/amplifying cards were each connected to Time-to-Digital (TDC) converters via ribbon cables. During the time period from October 2007 to February 2008 the discriminating/amplifying cards were connected to F1 TDC's mounted within two VME crates, each of which corresponded to a pair of drift chambers. However, during the data acquisition period when the HMS was at the small

forward angle of 14.495^o, it was noticed that the VME's were frequently crashing. It was hypothesized that the constant crashing could be due to an increase of radiation since at smaller angles the HMS hut was closer to the beam dump. If this turned out to be true, it would be of great concern due to the highest Q^2 point taking place at an HMS angle of 11.595^o. As a solution, the F1 TDC's were replaced with Lecroy 1877 TDC's mounted inside of a FastBus. The FastBus crate was also moved as far as possible from the Hall C beam dump while remaining inside the HMS hut. Even though the exact nature of the problem is still not fully understood, switching to a FastBus seem to greatly reduce the crashing.

The optimal threshold voltage applied to the discriminating/amplifying cards was found prior to the experiment using data taken detecting only cosmic rays. The upper and lower limits of -2.0 V and -4.0, respectively, placed on the threshold were based on errors which appeared on spectrum of hit rates per wire for each of the chambers. In the end, it was found that the best hit rates were being achieved at a threshold of -3.0 V, remaining at this voltage for most of the experiment.

The chambers were once again filled with a 50:50 mixture of argon/methane being supplied by the same external source used by the HMS. The gas lines were each connected to brass "T" dividers, resulting in a splitting of the line into two. One of the lines was connected to a filter in order to remove any impurities from the gas before it was fed into the chamber. The other served as a relief line in the case that the chamber pressure became too high. Both the relief line and the exhaust lines were connected to a bubbler filled with mineral oil. The bubbler served two purposes: to maintain a given pressure within the drift chamber and to provide enough backpressure to the relief line so as not to allow all of the gas to escape. Throughout the duration of the

experiment, the drift chambers were constantly being flushed with new gas at a rate of 200 cm^3/hour.

2.4.2 CH_2 Analyzer

In order to achieve the highest analyzing power, it would have been desirable to use pure LH_2 as the analyzer. However, the installation and operation of the necessary equipment required to maintain a tank of LH_2 would be cost ineffective and at times dangerous. Instead, polyethylene or CH_2 was chosen as a compromise between cost and analyzing power. Some significant properties of CH_2 are listed on Table 2.7[54].

Table 2.7: Relevant properties of CH_2

CH_2 Properties	
$\langle Z/A \rangle$	0.57034
$dE/dx\|_{min}$ [MeV/cm^{-1}]	1.850
Nuclear collision length λ_c [cm]	63.05
Nuclear interaction length λ_I [cm]	88.18
Radiation length X_0 [cm]	50.31

As was discussed in Chapter 1, the Dubna collaboration found that the analyzing power of CH_2 did not significantly increase by increasing the analyzer thickness beyond the nuclear collision length[13]. With this in mind, the thickness of the CH_2 analyzer was chosen to be 60 cm. Two analyzer blocks were used in order to increase the efficiency of the polarimeter in turn increasing the COM.

The blocks were capable of being manually extracted in order to allow the taking of straight through data at the beginning of each kinematic. This was crucial to the

[13]The nuclear collision length is defined as the mean free path of a particle before it interacts with the nuclei in a given material.

alignment of the drift chambers as well as their calibration. Furthermore, straight through data was used to find a proton signature within the HMSCal. The blocks were designed with a step in the middle which overlaps when closed. This was done in order to reduce the number of events which would otherwise go through the miniscule gap in between the analyzer blocks.

2.5 HMS Calorimeter

The use of the HMSCal originated from the curiosity of understanding its use to identify protons in single and multiple track events. The HMSCal is a TF1-000 lead glass calorimeter composed of 4 layers of thirteen blocks of dimension $10 \times 10 \times 70$ cm^3 as shown on Figure 2.9. Each block has a density of $\rho = 3.86$ g/cm^3, an index

Figure 2.9: Lead glass configuration of the HMS calorimeter.

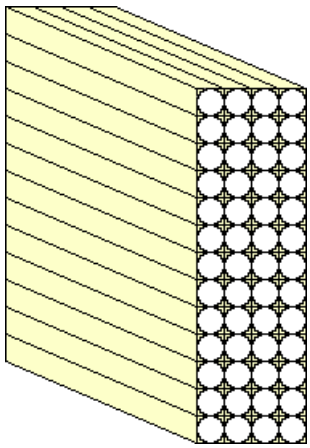

of refraction of $n = 1.65$ and a radiation length of $X_0 = 2.74$ cm. The chemical composition of TF1-000 can be found on Table 2.8[55].

Each of the blocks is surrounded by a layer of 25 μm aluminized Mylar and a 40 μm layer of Tedlar film. This ensures that the photons which are emitted within each

Table 2.8: The chemical structure of TF1-000 leaf glass.

TF1-000 Lead Glass	
Material	percentage
PbO	51.2
SiO_2	41.3
K_2O	7.0
As_2O_3	0.5

block do not escape to any of the surrounding blocks. Philips PMT X photomultiplier tubes are mounted on aluminum flanges located on either side of the blocks. The high voltage to the PMT's was provided by CAEN High Voltage modules. A detailed drawing of the calorimeter module is shown on Figure 2.10.

Figure 2.10: The HMS calorimeter module.

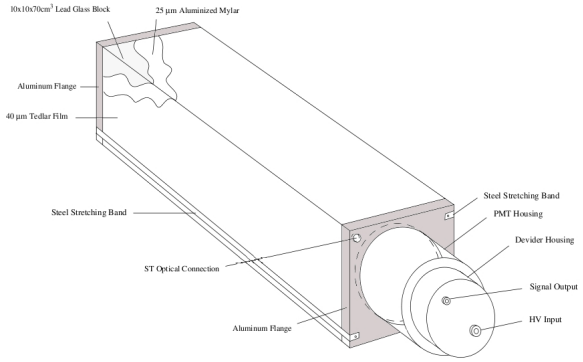

2.6 BigCal

Elastic electron-proton scattering event selection as well as electron shower position reconstruction was conducted using a lead glass calorimeter (BigCal). BigCal is an electromagnetic calorimeter composed of 1,744 bars of TF1-000 lead-glass (See

Table 2.8). The lead-glass bars used in the construction of the BigCal array were obtained from two different sources. The bottom array of 32 × 32 bars of dimension 3.8 cm × 3.8 cm × 45 cm were obtain from the Institute for High Energy Physics in Protvino, Russia. The top array of 30 × 24 bars of dimension 4.0 cm × 4.0 × × 40 were obtain from the Yerevan institute, in Armenia. The geometry of the lead glass bars and BigCal are shown on Figures 2.11 and 2.12.

Figure 2.11: The geometry of the lead glass bars.

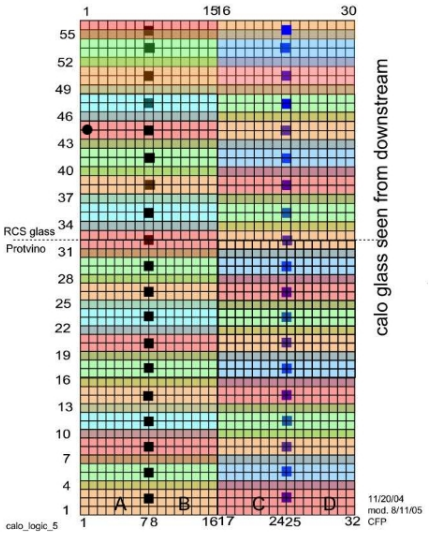

BigCal works on the principle of absorption. When the electron enters the lead glass of the calorimeter it interacts with the Coulomb field produced by the nuclei of the material. This causes the electron to change direction and in order to conserve energy it releases a Bremsstrahlung (breaking) photon. If the photon has a minimum energy of 1.22 MeV it will pair produce into a e^+e^- pairs which in turn radiate their own Bremsstrahlung photons. This process, known as an electromagnetic shower,

Figure 2.12: Overall geometry of BigCal.

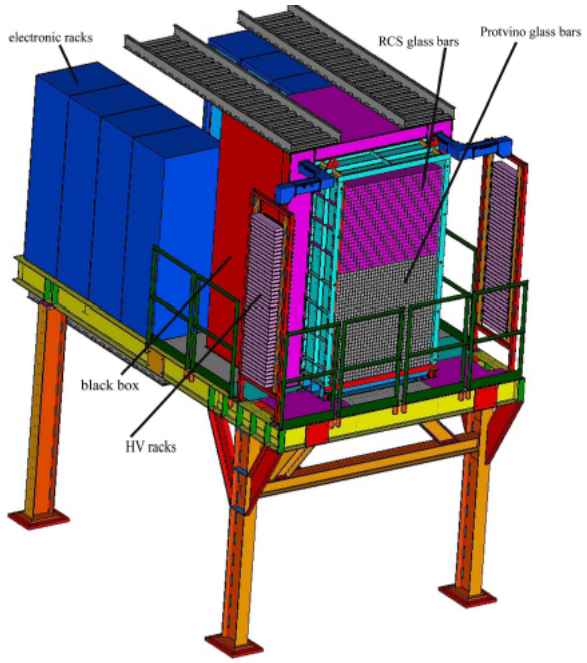

continues until the radiated photons fall below an energy of 1.22 MeV at which point they are absorbed by the lead glass bars. The particles produced in this process all travel faster than the speed of light of the material and as a result emit Cerenkov light. It is the Cerenkov photons which are detected by the PMT's which in turn produce a signal proportional to their energy.

The BigCal signals are collected using FEU84-12 photomultiplier tubes coupled to the ends of the of the lead glass bars. The analog signals produced by the PMT's were then integrated using LeCroy 1881M fastbus charge-integrating Analog-to-Digital converters (ADC). Each of the lead glass bars are insulated using Mylar wrapping in order to assure that the photons radiated within each bar do not escape to the

surrounding bars.

Chapter 3

Analysis

3.1 Elastic Event Selection

Even though coincidence detection of electrons and protons by BigCal and the HMS, respectively, eliminated a large amount of inelastic events, some still managed to get under the elastic peak as shown on Figure 3.1. Some of the electrons from

Figure 3.1: A plot of $[p - p_{el}(\theta_p)]/p^0$. The structure below the elastic peak is due to inelastic events which arose through processes where hard Bremsstrahlung photons, radiated within the target, were involved in either Compton scattering or π^0 photoproduction.

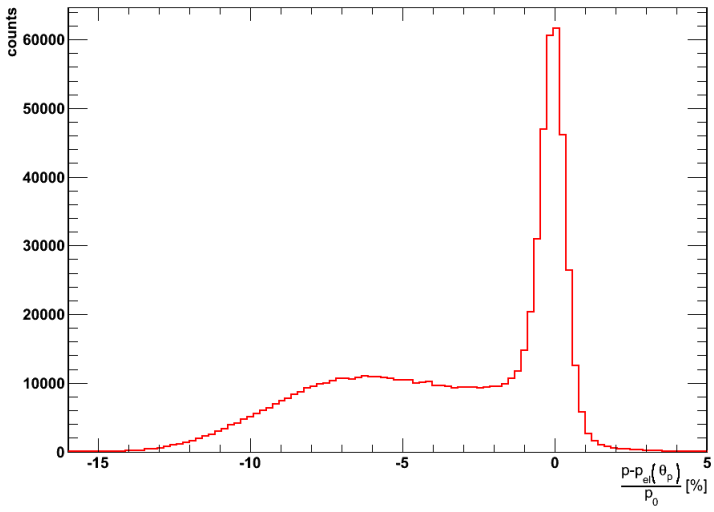

the beam, which entered the LH_2 target, Coulomb scattered with LH_2 nuclei. This in turn caused the electrons to accelerate releasing "Bremsstrahlung"[14] photons in order to conserve momentum.

[14]Bremsstrahlung is German for "braking radiation".

The inelastic events arose when hard Bremsstrahlung[15] photons either Compton scattered with the target nuclei ($\vec{\gamma}+p \rightarrow \gamma'+\vec{p}$) or were involved in π^0 photoproduction ($\vec{\gamma}+p \rightarrow \pi^0\ (\pi^0 \rightarrow \gamma+\gamma)+\vec{p}$). In both cases, the final state photons were able to make the trigger window and were misidentified as electrons by BigCal.

Figure 3.2: A plot of δ_x fit by a Crystal Ball function to describe the signal and a Gaussian to describe the background.

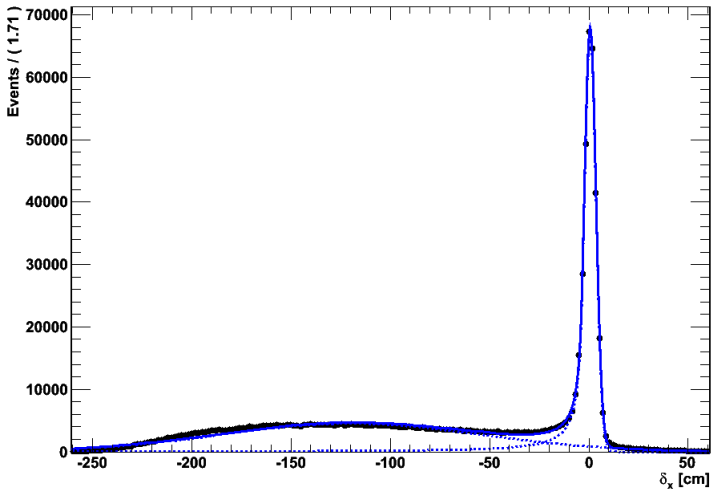

In order to discriminate between the remaining inelastic background and elastic events, a cut was applied to the correlation between the electron position measured by BigCal, $(x_{BC,e}, y_{BC,e})$, and that calculated using the proton position measured by the HMS $(x_{HMS,e}, y_{HMS,e})$. The electron position was calculated using two-body elastic

[15]Hard is used to denote Bremsstrahlung photons which have energies equal to or near the energies or the particles that radiate them.

Figure 3.3: A plot of δ_y fit by a Breit-Wigner to describe the signal and a Gaussian to describe the background.

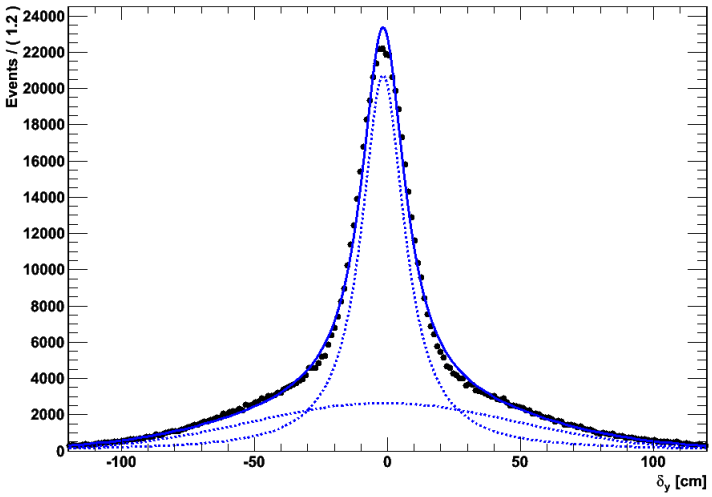

kinematics. The applied position correlation cut was of elliptical form

$$\sqrt{\left(\frac{\delta_x}{x_{cut}}\right)^2 + \left(\frac{\delta_y}{y_{cut}}\right)^2} < 1 \tag{3.1}$$

where

$$\delta_x = x_{BC,e} - x_{HMS,e} \tag{3.2}$$

$$\delta_y = y_{BC,e} - y_{HMS,e} \tag{3.3}$$

and (x_{cut}, y_{cut}) are the absolute values of the cuts applied to these quantities.

In order to choose the optimal cuts, δ_x and δ_y, were fit using the statistical package RooFit developed by David Kirkby of the University of California, Irvine and Wouter

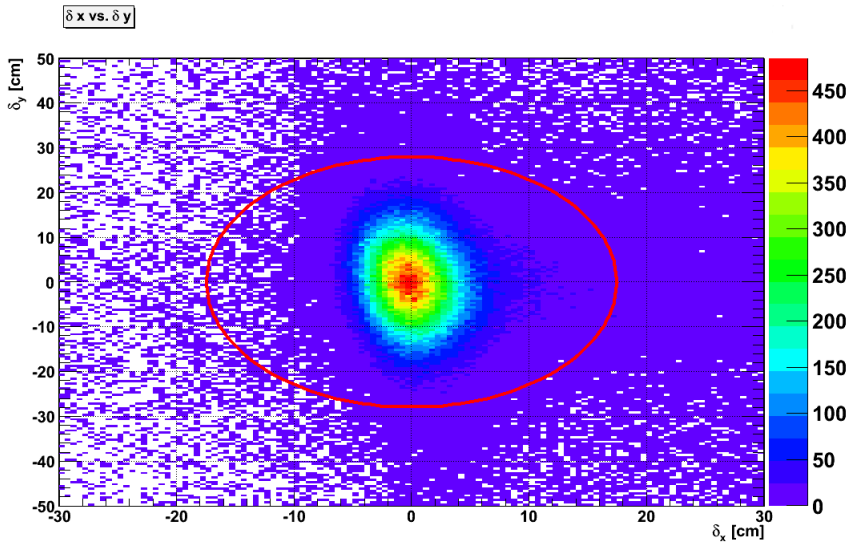

Figure 3.4: A plot outlining the elliptical cut that was placed on the position correlation.

Verkerke of the University of California, Santa Barbara [56]. δ_x was fit with a Crystal Ball function to describe the signal and a Gaussian to describe the background as shown on Figure 3.2. δ_y was fit with a Breit-Wigner function to describe the signal and a Gaussian to describe the background as shown on Figure 3.3. A description of the Breit-Wigner function is given in Appendix B. The result of these fits are listed on Table 3.1. It was concluded that applying a 5σ cut to δ_x corresponding to $x_{cut} = 17.50968$ cm and a cut to δ_y of $y_{cut} = 28$ cm resulted in the best elastic selection. The resulting elliptical cut is outlined on Figure 3.4 while the selection of elastic data is shown on Figure 3.5. The elastic peak was fit using a Breit-Wigner function yielding a resolution equal to $\sigma_{elastic}/p_0 \approx 5\%$.

3.2 FPP Track Reconstruction

	δ_x	δ_y	elastic peak
mean_{sig}	0.664197 cm	-1.68203 cm	-0.632452
σ_{sig}	2.91828 cm	19.6601 cm	1.1489
mean_{bkg}	-119.894 cm	-1.22000 cm	-
σ_{bkg}	65.5808 cm	50.000 cm	-

Table 3.1: Resulting mean and standard deviation for the fits done on δ_x, δ_y, and the elastic peak.

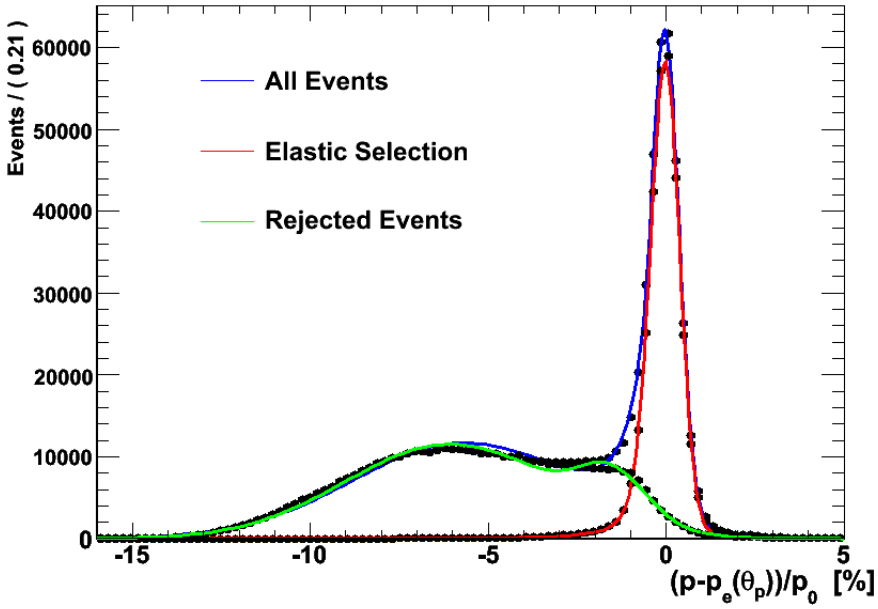

Figure 3.5: Final elastic selection.

Reconstruction of the charged particle tracks which emerge from the CH_2 analyzers begins with the determination of the drift times from the TDC information recorded for each hit. The data acquisition notes two instances in time for each event: the trigger time, t_{trig}, and the time a signal from a drift chamber wire arrives at the

TDC, t_{signal}. Each of these times does not necessarily correspond to the actual time of the event but to the time the signal was read out by the TDC's. As a result, various corrections need to be applied to each of the times before they can be used to calculate the drift time.

In order to determine the start time for the FPP drift chambers, the trigger time is first corrected to account for the pulse height of the signals delivered by the PMT's connected to the trigger scintillators. This accounts for differences in time required for signals of various pulse heights to overcome the TDC threshold. The trigger time is then corrected to account for the propagation of light from the origin of emittance of the signal through the scintillator bar. These two corrections give the time, $t_{corr.}$, when the proton crossed the scintillator hodoscope. The drift chamber start time, t_{start}, is then determined by projecting the corrected time, $t_{corr.}$, to the Focal Plane origin as

$$t_{start} = t_{corr.} - \frac{z}{v_p}$$

where z is the position of the hodoscopes relative to the Focal Plane origin and $v_p = \beta c$ is the velocity of the proton calculated using the HMS central momentum.

Once the drift chamber start time has been calculated, the drift time is found as

$$t_{drift} = t_{signal} - t_{start} + t_{cond.}(w_i)$$

where the conduction time is dependent on the position of the proton relative to the ith wire.

Next, an algorithm grouped the signals produced by the drift chamber wires (hits) into clusters consisting of a single hit and up to three adjacent hits. After all hits

have been grouped into clusters, the algorithm then linearly fits all combinations of a single cluster per plane based purely on the wire positions. The algorithm requires that at least five planes have clusters before it continues fitting ignoring those events which do not due to a lack of hits. A track found by the algorithm is considered "good" if it passes a cut placed on the χ^2 of the fit.

Those clusters which passed the first χ^2 test are then refitted using the drift time calculated for each hit. At this point, because an approximate position for each of the tracks is known, the conduction time correction is applied to the drift time of each of the hits. That combination of hits which gives the best χ^2 is then chosen as the correct track. Once all FPP tracks have been successfully reconstructed, they are used to extract the polar and azimuthal scattering angles of the proton emerging from the CH_2 analyzer.

3.3 Extraction of the Polarization Observables

3.3.1 Asymmetries

As was discussed in the opening chapter of this thesis, there exist an azimuthal scattering angle dependence on the polarization of a beam of particles incident on an analyzer due to the spin-orbit coupling term in the strong potential. Let us defined the coordinate system at the FPP to be as shown on Figure 3.6. For a large sample of polarized protons incident on a CH_2 analyzer, the azimuthal angular distribution for each of the helicity states ($\pm$) of the electron beam has been observed to be [57]

$$\begin{aligned} f^{\pm}(\theta,\phi) = \frac{1}{2\pi}[1 &+ (\pm hA_y(\theta)P_y^{fpp} + a_0)\cos\phi + (\mp hA_y(\theta)P_x^{fpp} + b_0)\sin\phi \\ &+ c_0\cos 2\phi + d_0\sin 2\phi + \ldots] \end{aligned} \tag{3.4}$$

Figure 3.6: The coordinate system as defined at the FPP drift chambers.

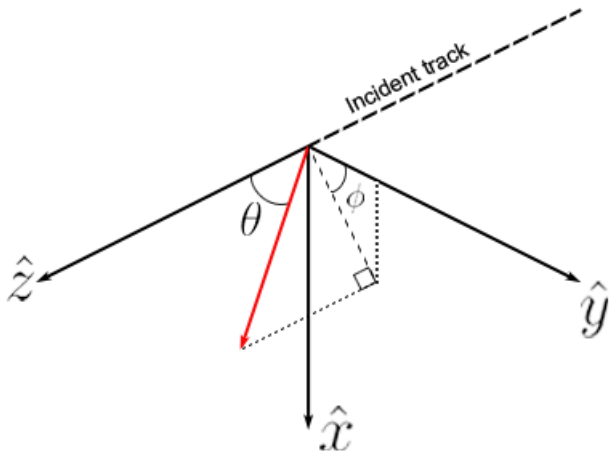

where h is the helicity of the electron beam, P_y^{fpp} and P_x^{fpp} are the components of the proton beam polarization at the FPP and (a_0, b_0, c_0, d_0) are constants representing the instrumental asymmetries of the FPP to second order. The instrumental asymmetries are a consequence of the imperfections of the FPP such as the possible misalignments of the drift chambers and the difference in efficiency of each of the drift chamber wires.

One of the inherent advantages of using a polarized electron beam is that the helicity state is flipped at a steady rate by the Pockel cells. This implies that the number of events in the positive and negative helicity states during a data acquisition period is basically the same. If it is assumed that the polarization of the electron beam did not significantly vary during the data acquisition period, then the probability distributions for the positive and negative helicity states are asymmetric in the polarization of the proton. If the sum of these distributions is taken, the polarization

Figure 3.7: The instrumental asymmetries obtain for $Q^2 = 2.733$ GeV^2. The instrumental asymmetries are due to imperfections that may be present in the FPP such as misalignments of the drift chambers and differences in the efficiency of the drift chamber wires.

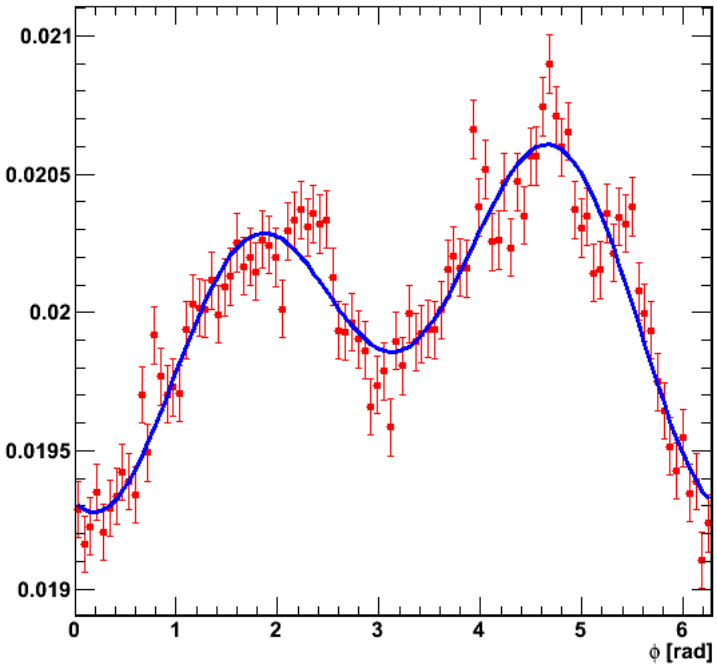

components will cancel leaving only the false asymmetries as

$$f^+ + f^- = \frac{1}{\pi}\left[1 + a_0 \cos\phi + b_0 \sin\phi + c_0 \cos 2\phi + d_0 \sin 2\phi + \ldots\right]. \qquad (3.5)$$

Fitting the sum distribution allows for the extraction of the parameters of equation (3.5). A plot of the instrumental asymmetries corresponding to data taken during kinematic 3 along with the resulting fit is shown on Figure 3.7. The resulting parameter values extracted from the fit are listed on Table 3.2.

Figure 3.8: Plot of the asymmetry in azimuthal scattering angle obtained from data collected for $Q^2 = 2.733$ GeV^2.

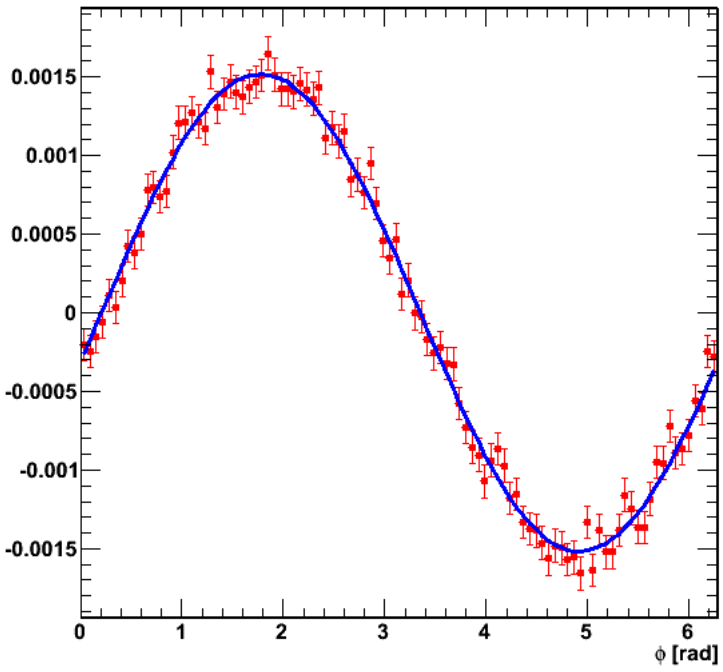

Table 3.2: The instrumental asymmetry fit parameters extracted from data collected for $Q^2 = 2.733$ GeV^2.

Parameter	value	error
a_0	-2.73291×10^{-4}	1.45849×10^{-5}
b_0	-1.91561×10^{-4}	1.47297×10^{-5}
a_0	-4.14330×10^{-4}	1.46449×10^{-5}
a_0	-8.57172×10^{-5}	1.46691×10^{-5}

If instead, the difference between the positive and negative helicity state distributions is taken, the instrumental asymmetries cancel leaving only the polarization observables

$$f^{+} - f^{-} = \frac{1}{\pi}\left(hA_y P_y^{fpp}\cos\phi - hA_y P_x^{fpp}\sin\phi\right). \tag{3.6}$$

Fitting this distribution allows for the extraction of $hA_y P_x^{fpp}$ and $hA_y P_y^{fpp}$ which is essentially[16] the components of the proton polarization at the FPP. The difference distribution for data collected at $Q^2 = 2.733$ GeV^2 is shown on Figure 3.8.

3.3.2 Spin Precession

Calculation of the form factor ratio cannot be simply accomplished with the use of the polarization observables extracted at the FPP. When the proton beam entered the HMS, its polarization precessed about the axis of the magnetic field due to its intrinsic magnetic moment. It then becomes necessary to model the proton beam interaction with the magnetic field as it propagated through the HMS which in turn can be used to extract the polarization observables at the target.

Since the magnetic field causes the polarization to rotate, the polarization of the proton at the target can be related its polarization at the FPP via a rotation matrix as follows

$$\begin{pmatrix} P_y^{fpp} \\ P_x^{fpp} \\ P_z^{fpp} \end{pmatrix} = \begin{pmatrix} S_{xx} & S_{xy} & S_{xz} \\ S_{yx} & S_{yy} & S_{yz} \\ S_{zx} & S_{zy} & S_{zz} \end{pmatrix} \begin{pmatrix} P_t \\ P_n \\ P_l \end{pmatrix}. \tag{3.7}$$

Since the polar and azimuthal angles of the scattered protons at the target are unique for each event, its trajectory through the HMS would also be distinct. This implies

[16] I say essentially because any constant in front of the polarization observables will not matter in the final calculation of the form factor ratio.

that the precession of the protons through the HMS must have also been different since each of the protons will experience a unique magnetic field. The coefficients must then be dependent on variables such as the position of the particle at the target and its momentum. In general, the coefficients can expanded as

$$S_{ij} = \sum_{k,l,m,n,p} C_{ij}^{klmnp} x^k \theta^l y^m \phi^n \delta^p \tag{3.8}$$

where C_{ij} are expansion coefficients, (x, y) are the cartesian coordinates of the proton at the target, (θ, ϕ) are the polar scattering angles and δ is defined as $\delta = (p_p - p_0)/p_0$.

The expansion coefficients were calculated by COSY, a program developed by Martin Berz of Michigan State University for the simulation and design optical particle systems [58]. COSY uses the geometry of the quadrupoles and dipole, the fringe fields of the dipole and the central momentum of the HMS to calculate the expansion coefficients to fifth order. COSY then outputs a table with the expansion coefficients which are then used to calculate the matrix coefficients for a given particle trajectory.

3.3.3 Maximum-likelihood Analysis

Consider a polarized beam of protons incident on one of the CH_2 analyzers. The probability that the ith proton will scatter within the analyzer by the angles θ_i and ϕ_i is given as

$$\begin{aligned} F_i(\theta_i, \phi_i) = \frac{1}{2\pi}[1 \quad &+ \quad \left(a_0 + hA_y(\theta_i) P_y^{fpp}\right) \cos\phi_i + \left(b_0 - hA_y(\theta_i) P_x^{fpp}\right) \sin\phi_i \\ &+ \quad c_0 \cos 2\phi_i + d_0 \sin 2\phi_i + \ldots]. \end{aligned} \tag{3.9}$$

The probability of obtaining a given angular distribution can then be obtained by

forming the product of all probabilities for each of the protons incident on the CH_2

$$\begin{aligned} F = \prod_{i=1}^{N} \frac{1}{2\pi}[1 \quad &+ \quad \left(a_0 + A_y(\theta_i)P_y^{fpp}\right)\cos\phi_i + \left(b_0 - A_y(\theta_i)P_x^{fpp}\right)\sin\phi_i \\ &+ \quad c_0\cos 2\phi_i + d_0\sin 2\phi_i + \ldots] \end{aligned} \tag{3.10}$$

where N is the total number protons. From equation (3.7) it is known that the polarization components at the FPP ($P_x^{fpp},\ P_y^{fpp}$) are related to their counterparts at the target as

$$\begin{aligned} P_x^{fpp} &= P_t S_{xx} + P_n S_{xy} + P_l S_{xz} \\ P_y^{fpp} &= P_t S_{yx} + P_n S_{yy} + P_l S_{yz}. \end{aligned} \tag{3.11}$$

Substitution of equation (3.11) into (3.10) yields the likelihood function in terms of the polarization observables at the target

$$\begin{aligned} \mathcal{L}(\vec{P}) = \prod_{i=1}^{N} \frac{1}{2\pi}[1 \quad &+ \quad (a_0 + \epsilon_i h A_y(\theta_i)(S_{yx,i}P_t + S_{yy,i}P_n + S_{yz,i}P_l))\cos\phi_i \\ &+ \quad (b_0 - \epsilon_i h A_y(\theta_i)(S_{xx,i}P_t + S_{xy,i}P_n + S_{xz,i}P_l))\sin\phi_i \\ &+ \quad c_0\cos 2\phi_i + d_0\sin 2\phi_i + \ldots] \end{aligned} \tag{3.12}$$

where ϵ_i is a constant which represents the sign of the helicity of the ith pro-

ton.Grouping like terms in P_t, P_n and P_l and defining the following

$$\begin{aligned}
\lambda_{0,i} &= a_0 \cos\phi_i + b_0 \sin\phi_i + c_0 \cos 2\phi_i + d_0 \sin 2\phi_i + \ldots \\
\lambda_{t,i} &= \epsilon_i h A_y(\theta_i)(S_{yx,i} \cos\phi_i - S_{xx,i} \sin\phi_i) \\
\lambda_{n,i} &= \epsilon_i h A_y(\theta_i)(S_{yy,i} \cos\phi_i - S_{xy,i} \sin\phi_i) \\
\lambda_{l,i} &= \epsilon_i h A_y(\theta_i)(S_{yz,i} \cos\phi_i - S_{xz,i} \sin\phi_i)
\end{aligned}$$

equation (3.12) can be rewritten as

$$\mathcal{L}(\vec{P}) = \prod_{i=i}^{N} \frac{1}{2\pi}(1 + \lambda_{0,i} + \lambda_{t,i} P_t + \lambda_{n,i} P_n + \lambda_{l,i} P_l). \tag{3.13}$$

The method of maximum-likelihood estimates the values of a set of parameters by finding values of those parameters which maximize the likelihood function. In the current case, the parameters (P_t, P_n, P_l) need to be chosen such that equation (3.13) is maximized. This can be done by taking the natural logarithm of and differentiating (3.13) with respect to P_t, P_n and P_l as

$$\frac{\partial \ln \mathcal{L}}{\partial P_j} = \frac{1}{2\pi} \sum_{i=0}^{N} \frac{\partial}{\partial P_j} \left(\ln(1 + \lambda_{0,i} + \lambda_{t,i} P_t + \lambda_{n,i} P_n + \lambda_{l,i} P_l)\right) \text{ for } j = l, n, t \tag{3.14}$$

yielding a set of coupled non-linear differential equations with no simple solutions[17].

In order to find a solution to the differential equations, equation (3.13) is Taylor

[17]It must be noted that the logarithm of equation (3.13) was taken in order to simplify the algebra involved when solving for the maxima. Since the logarithm of equation (3.13) is a continuous function over some range in the parameter space which strictly increases, those parameters which maximize the logarithm of the likelihood will also maximize the likelihood function itself.

expanded as

$$\ln(1+x) = x - \frac{x^2}{2} + \mathcal{O}(x^3).$$

where $x = \lambda_{0,i} + \lambda_{y,i} h P_y + \lambda_{z,i} h P_z$. Keeping terms to second order and differentiating as in equation (3.14) yields

$$\begin{pmatrix} \sum_i^N \lambda_{t,i}(1-\lambda_{0,i}) \\ \sum_i^N \lambda_{n,i}(1-\lambda_{0,i}) \\ \sum_i^N \lambda_{l,i}(1-\lambda_{0,i}) \end{pmatrix} = \begin{pmatrix} \sum_i^N \lambda_{t,i}\lambda_{t,i} & \sum_i^N \lambda_{t,i}\lambda_{n,i} & \sum_i^N \lambda_{t,i}\lambda_{l,i} \\ \sum_i^N \lambda_{n,i}\lambda_{t,i} & \sum_i^N \lambda_{n,i}\lambda_{n,i} & \sum_i^N \lambda_{n,i}\lambda_{l,x} \\ \sum_i^N \lambda_{l,i}\lambda_{t,i} & \sum_i^N \lambda_{l,i}\lambda_{n,i} & \sum_i^N \lambda_{l,i}\lambda_{l,x} \end{pmatrix} \begin{pmatrix} P_t \\ P_n \\ P_l \end{pmatrix}. \tag{3.15}$$

Letting the vector on the left hand side equal to $\mathbf{a}$ and the matrix on the right hand side equal to $\mathbf{P}$ the polarization observable are calculated as

$$\begin{pmatrix} P_t \\ P_n \\ P_l \end{pmatrix} = \mathbf{P^{-1}a} \tag{3.16}$$

with a statistical error given as

$$\Delta(P_t) = \sqrt{(P^{-1})_{tt}} \tag{3.17}$$

$$\Delta(P_n) = \sqrt{(P^{-1})_{nn}} \tag{3.18}$$

$$\Delta(P_l) = \sqrt{(P^{-1})_{ll}}. \tag{3.19}$$

3.4 Form Factor Ratio

Now that the polarization observables have been extracted at the target, the form

factor ratio can be calculated using equation (1.25) restated here for convenience

$$\mu_p \frac{G_E^p}{G_M^p} = -\frac{E_e + E_e'}{2m_p} \frac{P_t}{P_l} \tan\frac{\theta_e}{2}. \tag{3.20}$$

Letting $K = -\frac{E_e+E_e'}{2m_p} \tan\frac{\theta_e}{2}$, the statistical error of the ratio is defined as

$$\Delta\left(\frac{G_E^p}{G_M^p}\right) = K\left(\frac{1}{P_t^2}(\Delta P_l)^2 + \frac{P_l^2}{P_t^4}(\Delta P_t^2) - 2\frac{(P^{-1})_{tl}}{\sqrt{(P^{-1})_{tt}(P^{-1})_{ll}}}\frac{P_l}{P_t^3}\Delta P_l \Delta P_t\right)^{1/2}. \tag{3.21}$$

3.5 Analyzing Power Calibration

Another advantage of the Recoil Polarization Technique is that the polarization observables at the target can be written in terms of the form factor ratio as

$$\begin{aligned} P_l &= \frac{-2\sqrt{\tau(1+\tau)}\tan\frac{\theta_e}{2}\frac{G_E^p}{G_M^p}}{\left(\frac{G_E^p}{G_M^p}\right)^2 + \frac{\tau}{\epsilon}} \\ P_t &= \frac{\frac{E_e+E_e}{m_p}\sqrt{\tau(1+\tau)}\tan^2\frac{\theta_e}{2}}{\left(\frac{G_{Ep}}{G_{Mp}}\right)^2 + \frac{\tau}{\epsilon}}. \end{aligned} \tag{3.22}$$

As can be seen from equation (3.16), the analyzing power is required in order to calculate the polarization observables at the target. This implies that the calculated values of the polarization components at the target may not be the correct values but instead values proportional to them dependent on what analyzing power value is used. However, the value of the ratio of the polarization components is the correct one no matter what analyzing power values are used and is the reasoning why it is not needed to extract the form factor ratio.

If instead the analyzing power is initially assumed to be $A_y = 1$, then the values

of the polarization observables calculated by equation (3.16) are actually $A_y P_l$ and $A_y P_t$. Since the polarization observables can be extracted from equation (3.22) after the measurement of the analyzing power, then A_y can be extracted as

$$A_y = \alpha \frac{P_t^2}{P_l} + \beta P_l \tag{3.23}$$

$$\Delta A_y = \sqrt{\left(\frac{dA_y}{dP_t}\right)^2 (\Delta P_t)^2 + \left(\frac{dA_y}{dP_l}\right)^2 (\Delta P_l)^2 + 2\frac{(P^{-1})_{tl}}{\sqrt{(P^{-1})_{tt}(P^{-1})_{ll}}} \frac{dA_y}{dP_t} \Delta P_t \frac{dA_y}{dP_l} \Delta P_l} \tag{3.24}$$

where

$$\frac{dA_y}{dP_t} = 2\alpha \frac{P_t}{P_l} \tag{3.25}$$

$$\frac{dA_y}{dP_l} = -\alpha \left(\frac{P_t}{P_l}\right)^2 + \beta \tag{3.26}$$

$$\alpha = \frac{E_e + E_{e'}}{h 4 m_p \sqrt{\tau(1+\tau)}} \tag{3.27}$$

$$\beta = \frac{\tau \left[1 + 2(1+\tau)\tan^2\left(\frac{\theta_e}{2}\right)\right]}{h \frac{E_e + E'_e}{m_p} \sqrt{\tau(1+\tau)\tan^2\left(\frac{\theta_e}{2}\right)}}. \tag{3.28}$$

3.6 Proton Identification

As higher proton momenta are achieved, multiple tracks events emerging from the CH_2 become more prominent. This will especially become a problem during the next round of form factor ratio measurements which will take place with an electron beam of 11 GeV up to a $Q^2 = 13$ GeV^2. Since the proton azimuthal and

polar scattering angles are required for the calculation of its polarization, it would be desirable to be able to identify which of the tracks emerging from the CH_2 is associated with the proton. Furthermore, identification of the proton track will lead to much higher analyzing powers than those currently observed with multi track events in turn improving the uncertainty in the form factor ratio.

Use of the HMSCal as a means of possible particle identification was not originally intended by the G_E^p-III collaboration. As a result, calibration of the HMSCal energy was never attempted and datum was not readily available to perform it. In fact, the only information available per event was the position of the lead glass bars which read out a signal, the total number of hits in the calorimeter per event, and the integrated

Figure 3.9: Proton ADC signature obtained using straight through data in which the analyzers were removed.

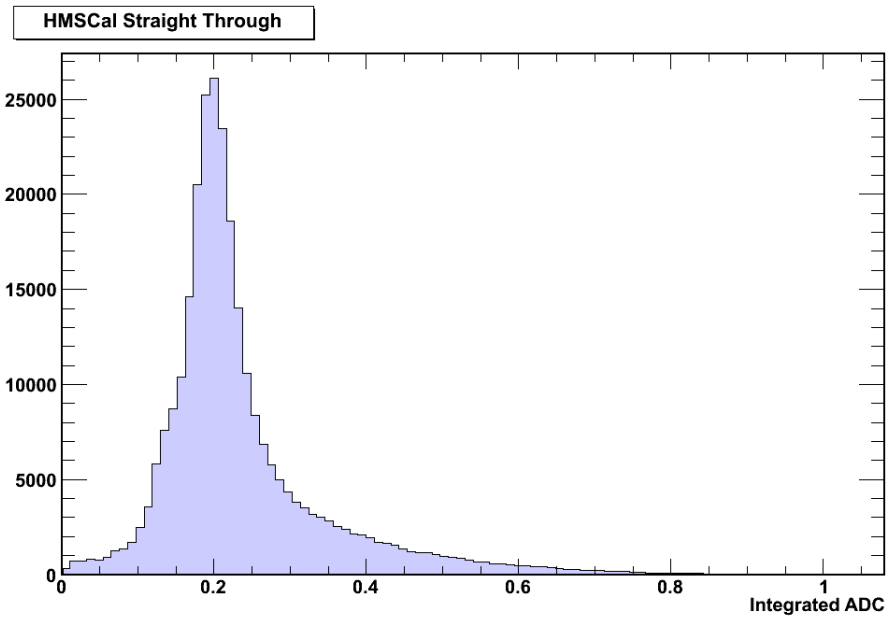

ADC values per layer. To further complicate things, the lead glass bars spanned the total horizontal acceptance of the HMSCal leading to poor position resolution along HMSCal's horizontal direction. This became a common problem when attempting to assign HMS shower clusters to tracks which entered and exited the HMSCal through the same bars.

Instead, a proton signature was sought after in the total ADC spectra of an event using data collected with the analyzers removed. The ADC spectra revealed a clean peak which is characteristic of a single proton entering the HMSCal. The peak is shown on Figure 3.9.

Figure 3.10: FPP2 single track calorimeter selections. The selection outlined in red was achieved by requiring at least four hits in the calorimeter and that selection outlined in blue was achieved by requiring less than 4 hits in the calorimeter.

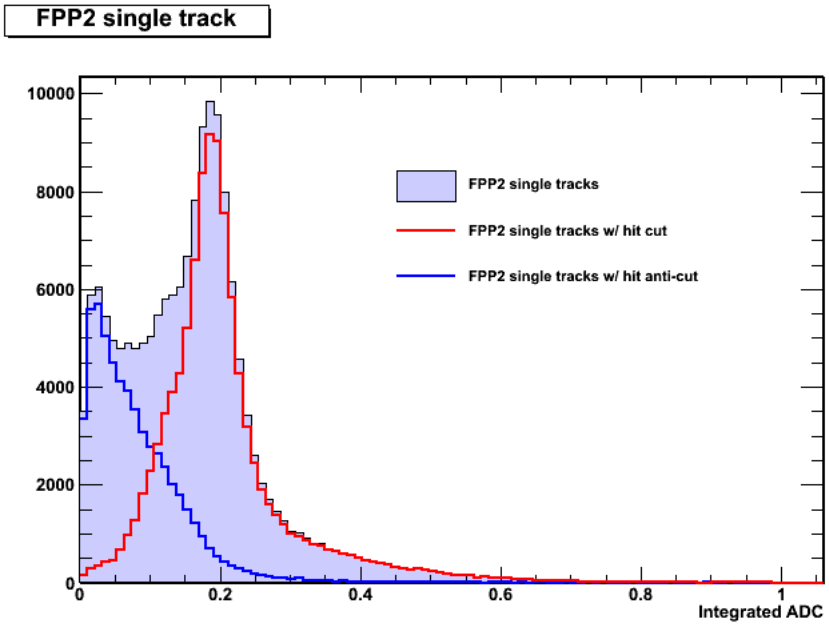

Similar proton signatures were observed in ADC spectra of data taken with the

polarimeters in. However, another characteristic peak began to appear at a lower ADC value. It was suggested that this peak could belong to neutrons and a possible way of identifying them would be to look at the number of hits in HMSCal. Neutrons which enter the calorimeter will take longer to interact with nuclei in the glass bars resulting in a smaller number of calorimeter hits. By requiring that an event have

Figure 3.11: FPP2 multiple track calorimeter selections. The selection outlined in red was achieved by requiring at least four hits in the calorimeter and that selection outlined in blue was achieved by requiring less than 4 hits in the calorimeter.

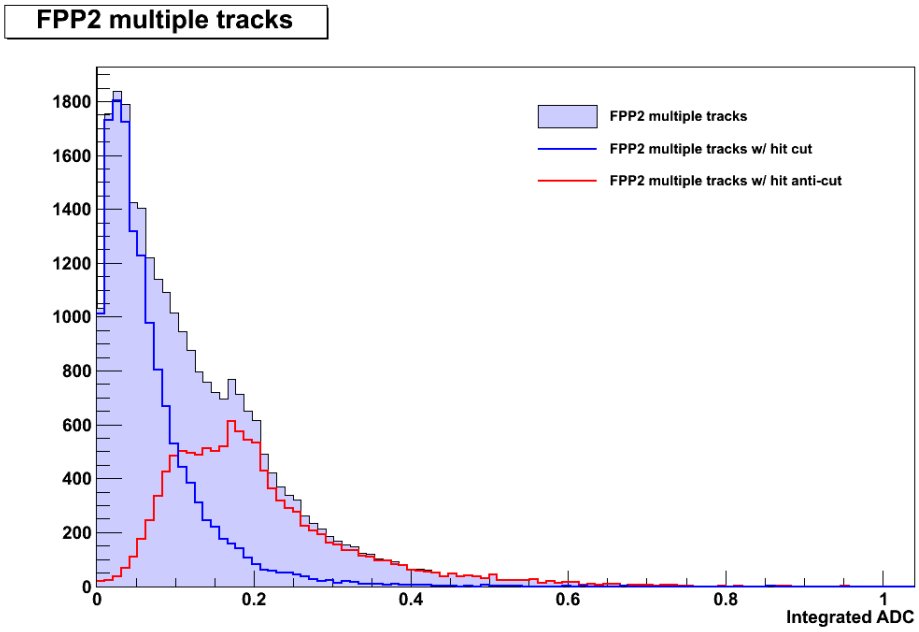

at least 4 hits in the calorimeter corresponding to one hit per layer, what had been identified as the proton peak was successfully isolated. The particular calorimeter selection achieved by imposing the hit requirement are shown in red on Figure for single tracks emerging from FPP2 and for multiple tracks on Figure . The selections chosen in blue are those achieved by requiring less than 4 hits in the calorimeter. As

can be seen from the figures, this cut successfully extracted the peak at the lower ADC values. This verifies the hypothesis that the peak likely belongs to neutrons.

Chapter 4

Results and Discussion

4.1 Analyzing Power

The multi polarimeter setup of the FPP allowed for an independent measurement of the analyzing power for each of the polarimeters for the conditions outlined on Table 4.1.

Table 4.1: Track conditions at which the analyzing power was measured.

	FPP1 # Tracks	FPP2 # Tracks
FPP1 All	>= 1	>= 1
FPP2 All	>= 1	>= 1
FPP1 Single	1	>= 1
FPP2 Single	>= 1	1
FPP1 Multiple	> 1	>= 1
FPP2 Multiple	>= 1	> 1

The analyzing power measurements obtained using the method described in Chapter 3 are shown on Figure 4.1 along with the analyzing power predicted by the Dubna parametrization[18]. The analyzing power measurements made for all tracks seem to agree with that predicted from the Dubna parametrization. This was expected since Dubna made no explicit identification of any final state tracks in their measurements.

The analyzing powers were fit to the parametrization

$$A(p_t) = p_0 p_t e^{-p_1 p_t^2} \tag{4.1}$$

[18]It must be noted that the analyzing powers are plotted against the transverse momentum, $p_t = p_p \sin\theta_{fpp}$, in order to allow them to be on the same plot. As a consequence, what is shown on Figure 4.1 is not the real analyzing power but is proportional to it and has the same dependence on the transverse momentum.

Figure 4.1: Analyzing power measurements for the reaction $p + CH_2$ at a proton momentum of 2.2032 GeV. The analyzing power was measured for the conditions described on Table 4.1

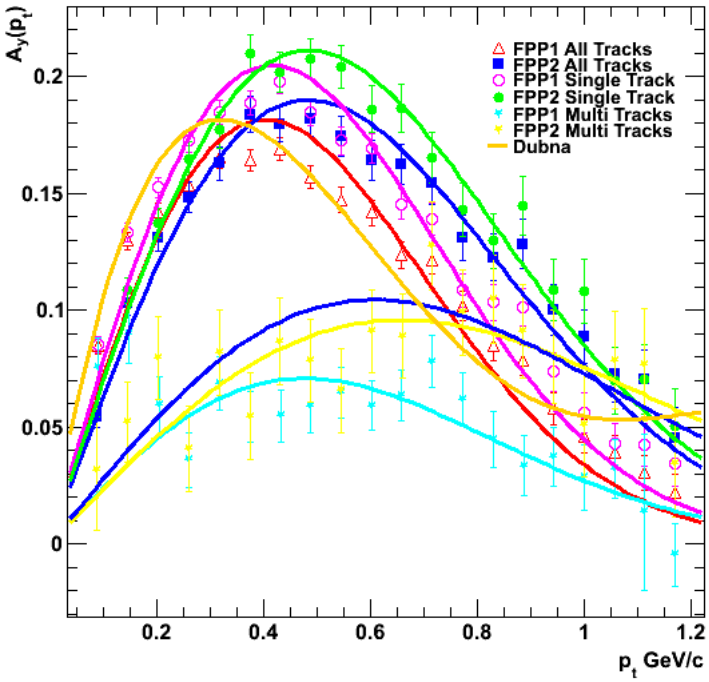

where p_0 and p_1 are parameters and p_t is the transverse momentum of the proton defined as

$$p_t = p_p \sin\theta_{fpp}.$$

The results of these fits are listed on Table 4.2. From the figure it immediately follows that the highest analyzing power was obtained by using single track events. This was expected because it is reasonable to assume that a single track emerging from the analyzer will in most cases be a proton. Furthermore, the measurement does not

Table 4.2: Results of the fit to the analyzing powers.

	p_0	p_1
FPP1 All	$0.743467 \pm 1.09767 \times 10^{-2}$	$3.09213 \pm 5.86570 \times 10^{-2}$
FPP2 All	$0.647346 \pm 1.31554 \times 10^{-2}$	$2.14150 \pm 5.98798 \times 10^{-2}$
FPP1 Single	$0.813728 \pm 1.14991 \times 10^{-2}$	$2.90842 \pm 5.55607 \times 10^{-2}$
FPP2 Single	$0.719325 \pm 1.43274 \times 10^{-2}$	$2.13786 \pm 6.09922 \times 10^{-2}$
FPP1 Multiple	$0.247789 \pm 2.16109 \times 10^{-2}$	$2.20683 \pm 2.22055 \times 10^{-1}$
FPP2 Multiple	$0.240072 \pm 2.36551 \times 10^{-2}$	$1.15792 \pm 1.66415 \times 10^{-1}$

make use of multiple track events which have a very low analyzing power. It is also interesting to note that the analyzing power of the second focal plane polarimeter is slightly higher than that of the first. This is likely due to the unaccounted energy losses that the protons experienced as they passed through the first polarimeter.

4.2 HMS Calorimeter Selection

Using the HMS calorimeter to identify "neutrons" has lead to a statistical increase in the analyzing power of both single track and multiple track events emerging from FPP2[19]. The analyzing power for single track events in FPP2 with and without the cut on the number of hits present in HMSCal is shown on Figure 4.2.

The large error present in the measurements using the HMSCal cut were simply due to a lack of statistics. The anticut analyzing power refers to that obtained from the identified neutrons. The observed increase in the analyzing power is likely due to the elimination of events which contain a proton-neutron final state. However, there is also an indication that those events which contain a neutron final state also have an analyzing power. At this point, it is not fully clear if this is due to the large overlap

[19]The calorimeter studies excluded tracks emerging from FPP1 since their interaction in FPP2 could not be modeled.

Figure 4.2: Comparison of analyzing power measurements between FPP2 single track events with and without the HMSCal restriction on the number of hits. The analyzing power of events which did not pass the HMSCal hit restriction is also shown.

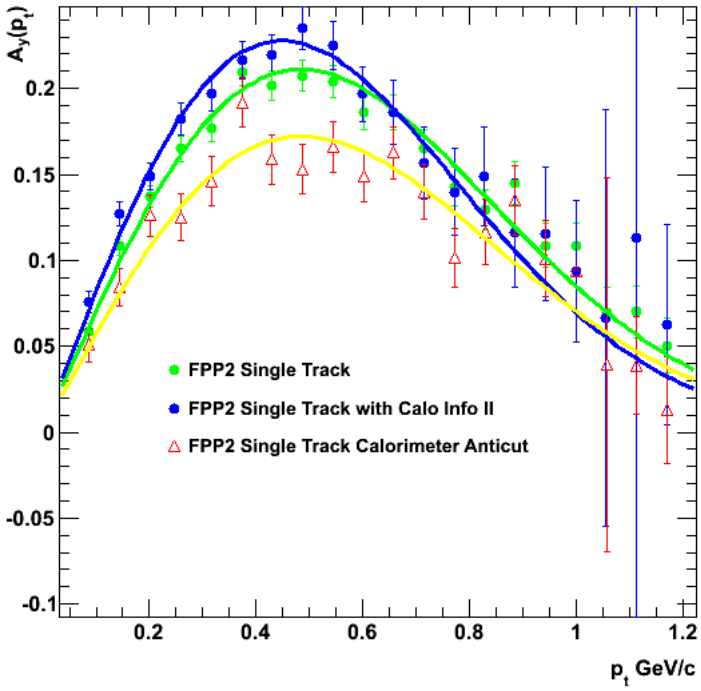

between the proton and neutron peak or if it is simply due to the neutrons having an analyzing power. Not much information is available as to the neutron analyzing power making it difficult to reach a clear conclusion.

A similar increase in the analyzing power of multiple track events was also observed as shown on Figure 4.3. The lack of statistics when looking at multi track events make its difficult to conclude if the HMSCal selection made a meaningful contribution to the analyzing power. Going strictly from the fit, however, a reasonable increased is noticed.

Figure 4.3: The analyzing power for multiple track events which emerge from the second polarimeter with and without the calorimeter cut.

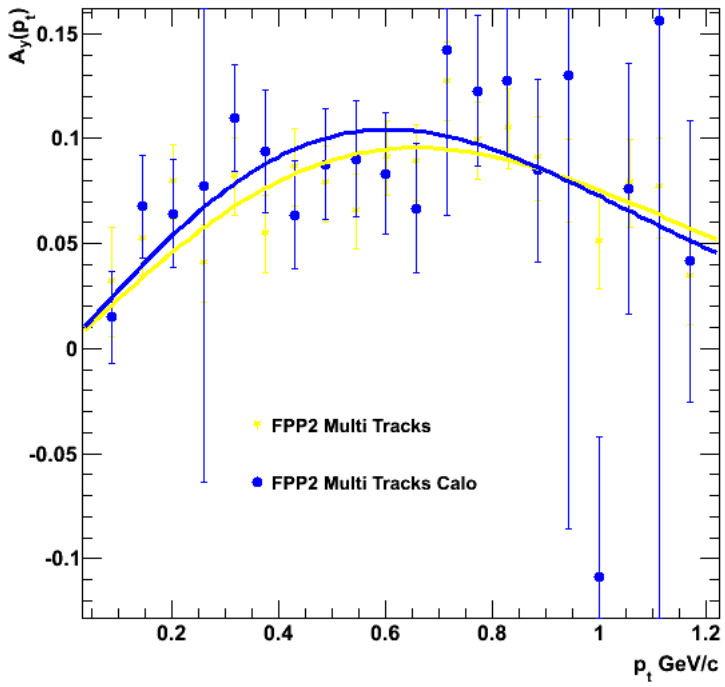

4.3 G_E^P/G_M^p Measurement

The extracted form factor measurement for the $Q^2 = 2.773$ GeV^2 along with those made by the $G_E^p - I$ and $G_E^p - II$ are shown on Figure 4.4. The value was calculated by taking a weighted average of the FPP1 and FPP2 single track measurements. As can be seen from the figure, the measurement made at $Q^2 = 2.733$ GeV^2 agrees very well with those measurements made by $G_E^p - I$ in Hall A. This serves as a validation of the Recoil Polarization Technique.

4.4 Conclusion

Figure 4.4: Measurement of $\mu G_E^p/G_M^p$ for the $Q^2 = 2.733 GeV^s$ point compared to measurements made by G_E^p-I and G_E^p-II.

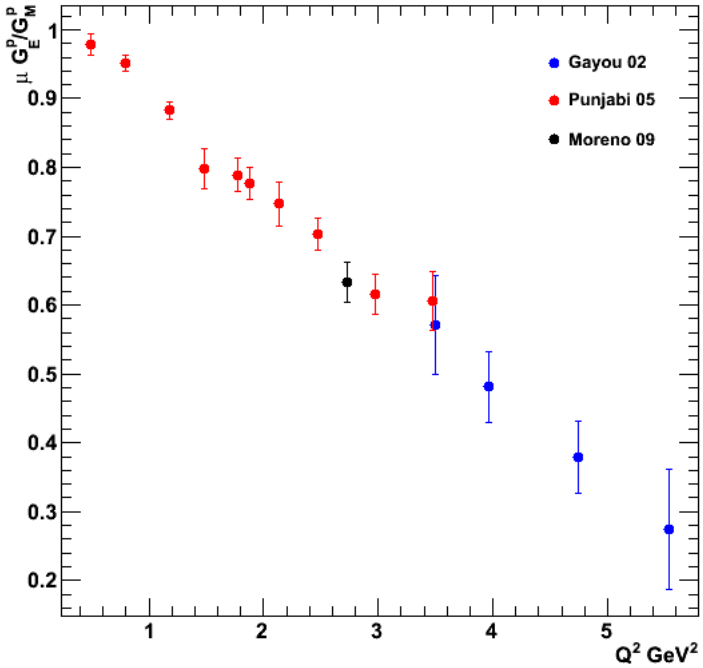

In conclusion, use of a calorimeter to identify final state particles is a potential way to increase the analyzing power. There are several ways to improve the identification of particle emerging from FPP2. One is to do the energy calibration of the calorimeter.

One of the major obstacles of this analysis is the fact that the in plane spatial resolution of the calorimeter was very poor. This limited the number of clusters that could be matched to tracks emerging from FPP2 and in turn limited the analysis to single track events. An improvement in resolution can be achieved by placing a scintillator hodoscope in front of the calorimeter.

The identification of the neutron and gamma rays is a bit more difficult. The neutrons, for example, will not leave a signal in the scintillator hodoscopes. If clusters in the calorimeter are found not to have a matching track in FPP2 and no signal in the scintillator hodoscope then it is most likely a neutron or a gamma ray. If the energy calibration of the calorimeter is done, then the gamma ray signature would be much cleaner. In order to best understand what suggested modifications would lead to the best results, Monte Carlo simulations should be done using the proton momenta expected for G_E^p-IV.

Finally, the excellent agreement between the previous Hall A form factor measurement and the one presented in this paper gives further merit to the Recoil Polarization Technique.

References

[1] J. Chadwick. Possible Existence of the Neutron. *Nature*, 129(3252):312, 1932.

[2] L. W. Alvarez and F. Bloch. A Quantitative Determination of the Neutron Moment in Absolute Nuclear Magnetons. *Phys. Rev.*, 57(2):111–122, 1940.

[3] I. Estermann et al. The Magnetic Moment of the Proton. *Phys. Rev.*, 52(6):535–545, 1937.

[4] M. Gell-Mann. A Schematic Model of Baryon and Mesons. *Phys. Lett.*, 8:214–215, 1964.

[5] G. Zweig. An SU(3) Model for Strong Interaction Symmetry and its Breaking: Part II. *CERN-TH-412*, 1964.

[6] E. D. Bloom et al. High-Energy Inelastic $e - p$ Scattering at 6^o and 10^o. *Phys. Rev. Lett.*, 23(16):930–934, 1969.

[7] M. Breidenbach et al. Observed Behavior of Highly Inelastic Electron-Proton Scattering. *Phys. Rev. Lett.*, 23(16):935–939, 1969.

[8] F. Abe et al. Observation of Top Quark Production in $p\bar{p}$ Collisions with the Collider Detector at Fermilab. *Phys. Rev. Lett.*, 74(14):2626–2631, 1995.

[9] S. Abachi et al. Search for High Mass Top Quark Production in $p\bar{p}$ Collisions at $s = 1.8$ TeV. *Phys. Rev. Lett.*, 74(13):2422–2426, 1995.

[10] D. J. Griffiths. Introduction to Elementary Particles. *John Wiley & Sons, Inc.*, 262–267, 1987.

[11] C. F. Perdrisat, Punjabi V., and Vanderhaeghen M. Nucleon Electromagnetic Form Factors. *Progress in Particle and Nuclear Physics*, 59(2):694 – 764, 2007.

[12] J. J. Kelly. Nucleon Charge and Magnetization Densities from Sachs Form Form Factors. *Phys. Rev. C*, 66(6):065203, 2002.

[13] O. Gayou. Measurement of the Proton Form Factor Ratio $\mu G_E^p/G_M^p$ Up to $Q^2 = 5.6$ GeV^2 By Recoil Polarimetry. *A thesis submitted to The College of William and Mary*, 31, 2002.

[14] L. Andivahis et al. Measurements of the Electric and Magnetic Form Factors of the Proton from Q^2=1.75 to 8.83 GeV/^{2}. *Phys. Rev. D*, 50(9):5491–5517, 1994.

[15] R. G. Sachs. The Physics of Time Reversal. *University of Chicago Press*, 1987.

[16] O. Gayou. Measurement of the Proton Form Factor Ratio $\mu G_E^p/G_M^p$ Up to $Q^2 = 5.6$ GeV^2 By Recoil Polarimetry. *A thesis submitted to The College of William and Mary*, 134, 2002.

[17] L. N. Hand, D. G. Miller, and Richard Wilson. Electric and Magnetic Form Factors of the Nucleon. *Rev. Mod. Phys.*, 35(2):335–349, 1963.

[18] L. E. Price et al. Backward-Angle Electron-Proton Elastic Scattering and Proton Electromagnetic Form Factors. *Phys. Rev. D*, 4(1):45–53, 1971.

[19] J. Litt et al. Measurement of the Ratio of the Proton Form Factors, G_E/G_M, at High Momentum Transfers and the Question of Scaling. *Phys. Lett. B*, 31(1):40 – 44, 1970.

[20] W. Bartel et al. Measurement of Proton and Neutron Electromagnetic Form Factors at Squared Four-Momentum Transfers Up to 3 GeV^2/c. *Nuclear Physics B*, 58(2):429 – 475, 1973.

[21] C. Berger et al. Electromagnetic Form Factors of the Proton at Squared Four-Momentum Transfers Between 10 and 50 fm^{-2}. *Phys. Lett. B*, 35(1):87 – 89, 1971.

[22] K. M Hanson et al. Large-Angle Quasielastic Electron-Deuteron Scattering. *Phys. Rev. D*, 8(3):753–778, 1973.

[23] F. Borkowski et al. Electromagnetic Form Factors of the Proton at Low Four-Momentum Transfer (II). *Nuclear Physics B*, 93(3):461 – 478, 1975.

[24] G. G. Simon et al. Absolute Electron-Proton Cross Sections at Low Momentum Transfer Measured with a High Pressure Gas Target System. *Nuclear Physics A*, 333(3):381 – 391, 1980.

[25] R. C. Walker et al. Measurements of the Proton Elastic Form Factors for $1 \leq Q^2 \leq 3$ $(GeV/c)^2$ at SLAC. *Phys. Rev. D*, 49(11):5671–5689, 1994.

[26] I. A. Qattan et al. Precision Rosenbluth Measurement of the Proton Elastic Form Factors. *Phys. Rev. Lett.*, 94(14):142301, 2005.

[27] M. E. Christy et al. Measurements of Electron-Proton Elastic Cross Sections for $0.4 < Q^2 < 5.5$ $(GeV/c)^2$. *Phys. Rev. C*, 70(1):015206, 2004.

[28] T. Janssens et al. Proton Form Factors from Elastic Electron-Proton Scattering. *Phys. Rev.*, 142(4):922–931, 1966.

[29] D. H. Coward et al. Electron-Proton Elastic Scattering at High Momentum Transfers. *Phys. Rev. Lett.*, 20(6):292–295, 1968.

[30] A. F. Sill et al. Measurements of Elastic Electron-Proton Scattering at Large Momentum Transfer. *Phys. Rev. D*, 48(1):29–55, 1993.

[31] O. Gayou et al. Measurements of the Elastic Electromagnetic Form Factor Fatio $\mu_p G_E^p/G_M^p$ Via Polarization Transfer. *Phys. Rev. C*, 64(3):038202, 2001.

[32] O. Gayou et al. Measurement of G_E^p/G_M^p in $ep \rightarrow ep$ to $Q^2 = 5.6$ GeV^2. *Phys. Rev. Lett.*, 88:092301, 2002.

[33] V. Punjabi et al. Proton Elastic Form Factor Ratios to $Q^2 = 3.5\ GeV^2$ by Polarization Transfer. *Phys. Rev. C*, 71(5):055202, 2005.

[34] B. D. Milbrath. A Comparison of Polarization Observables in Electron Scattering from the Proton and Deuteron. *ERRATUM-IBID.*, 82:2221, 1999.

[35] S. Dieterich et al. Polarization Transfer in the ^{4}He$(\vec{e}, e'\vec{p})^3$H Reaction. *Phys. Lett. B*, 500:47, 2001.

[36] S. Strauch and S. Dieterich. Polarization Transfer in the ^{4}He$(\vec{e}, e'\vec{p})^3$H Reaction up to $Q^2 = 2.6$ (GeV/c)^2. *Phys. Rev. Lett.*, 91(5):052301, 2003.

[37] B. Hu et al. Polarization Transfer in the ^{2}H$(\vec{e}, e'\vec{p})n$ Reaction Up to $Q^2 = 1.61$ (GeV/c)^2. *Phy. Rev. C*, 73(6):064004, 2006.

[38] M. K. Jones. Proton G_E/G_M from Beam-Target Asymmetry. *Phys. Rev. C*, 74:035201, 2006.

[39] G. MacLachlan et al. The Ratio of Proton Electromagnetic Form Factors Via Recoil Polarimetry at $Q^2 = 1.13$ (GeV/c)^2. *Nuclear Physics A*, 764:261 – 273, 2006.

[40] Th. Pospischil et al. Measurement of G_E^p/G_M^p via Polarization Transfer at $Q^2 = 0.4$ GeV/c^2. *The European Physical Journal A - Hadrons and Nuclei*, 12(1):125–127, 2001.

[41] L. S. Azhgirey. Measurement of Analyzing Powers for the Reaction $\vec{p}$+CH_2 at $p_p = 1.75 - 5.3$ GeV/c . *Nuclear Instruments and Methods in Physics Research Section A: Accelerators, Spectrometers, Detectors and Associated Equipment*, 538(1-3):431 – 441, 2005.

[42] T. Maruyama et al. Systematic Study of Polarized Electron Emission from Strained GaAs/GaAsP Superlattice Photocathodes. *App. Phys. Lett.*, 85(13):2640–2642, 2004.

[43] J. Hansknecht and M. Poelker. Synchronous Photoinjection Using a Frequency-Doubled Gain-Switched Fiber-Coupled Seed Laser and ErYb-Doped Fiber Amplifier. *Phys. Rev. ST Accel. Beams*, 9(6):063501, 2006.

[44] P. Kneisel et al. Performance of Superconducting Cavities for CEBAF. *Particle Accelerator Conference, Proceedings of the 1993*, 2:1396–1398, 1993.

[45] C. Yan, R. Carlini, and D. Neuffer. Beam Energy Measurement Using the Hall C Beamline (CEBAF). *Particle Accelerator Conference, Proceedings of the 1993*, 3:2136–2138, 1993.

[46] M. Hauger et al. A High-Precision Polarimeter. *Nuclear Instruments and Methods in Physics Research Section A: Accelerators,Spectrometers,Detectors and Associated Equipment*, 462(3):382 – 392, 2001.

[47] L. Tang, C. Yan, and Ed. V. Hungerford. Systematic Resolution Study of the CEBAF Hall C Spectrometers – HMS and SOS. *Nuclear Instruments and Methods in Physics Research Section A: Accelerators, Spectrometers, Detectors and Associated Equipment*, 366(2-3):259 – 262, 1995.

[48] S. R. Lassiter et al. Final Design and Construction Progress for CEBAF's Cold Iron Quadrupoles. *Applied Superconductivity, IEEE Transactions on*, 3(1):118–121, 1993.

[49] P. Bogensberger et al. Design and Manufacture of the Dipole Coil for the CEBAF High Momentum Spectrometer. *Applied Superconductivity, IEEE Transactions on*, 3(1):797–800, 1993.

[50] W. Blum, W. Riegler, and L. Rolandi. Particle Detection with Drift Chambers. *Springer*, 2008.

[51] O. K. Baker et al. The High Momentum Spectrometer Drift Chambers in Hall C at CEBAF. *Nuclear Instruments and Methods in Physics Research Section A: Accelerators, Spectrometers, Detectors and Associated Equipment*, 367(1-3):92 – 95, 1995.

[52] B. Jean-Marie, V. Lepeltier, and D. L'Hote. Systematic Measurement of Electron Drift Velocity and Study of Some Properties of Four Gas Mixtures: A—CH4,

A—C2H4, A—C2H6, A—C3H8. *Nuclear Instruments and Methods*, 159(1):213 – 219, 1979.

[53] D. Abbott et al. The High Momentum Spectrometer Drift Chambers. *CEBAF 1992 Summer Workshop*, 269:495–498, 1992.

[54] D. E. Groom. Atomic and Nuclear Properties of Materials. *Particle Data Book*, 2007.

[55] M. Y. Balatz et al. The Lead-Glass Electromagnetic Calorimeter for the SELEX Experiment. *Nuclear Instruments and Methods in Physics Research Section A: Accelerators, Spectrometers, Detectors and Associated Equipment*, 545(1-2):114 – 138, 2005.

[56] W. Verkerke and D. Kirkby. The RooFit Toolkit for Data Modeling. *SLAC physics/0306116*, 2003.

[57] O. Gayou. Measurement of the Proton Form Factor Ratio $\mu G_E^p/G_M^p$ Up to $Q^2 = 5.6$ GeV^2 By Recoil Polarimetry. *A thesis submitted to The College of William and Mary*, 31, 2002.

[58] K. Makino and M. Berz. Cosy Infinity Version 8. *Nuclear Instrumentation and Methods in Physics Research Section A*, 427:338, 1999.

[59] J. Gaiser. Charmonium Spectroscopy from Radiative Decays of the J/ψ and ψ'. *SLAC-0255*, 178, 1982.

Appendix A

Definitions

A.1 Minkowski Metric

The Minkowski metric is represented by the matrix

$$g_{\mu\nu} = \begin{pmatrix} -1 & 0 & 0 & 0 \\ 0 & 1 & 0 & 0 \\ 0 & 0 & 1 & 0 \\ 0 & 0 & 0 & 1 \end{pmatrix}. \tag{A.1}$$

A.2 Gamma Matrices

The Dirac γ-matrices are defined as follows

$$\gamma^0 = \begin{pmatrix} 1 & 0 & 0 & 0 \\ 0 & 1 & 0 & 0 \\ 0 & 0 & -1 & 0 \\ 0 & 0 & 0 & -1 \end{pmatrix} \quad \gamma^1 = \begin{pmatrix} 0 & 0 & 0 & 1 \\ 0 & 0 & 1 & 0 \\ 0 & -1 & 0 & 0 \\ -1 & 0 & 0 & 0 \end{pmatrix}$$

$$\gamma^2 = \begin{pmatrix} 0 & 0 & 0 & -i \\ 0 & 0 & -i & 0 \\ 0 & -i & 0 & 0 \\ -i & 0 & 0 & 0 \end{pmatrix} \quad \gamma^3 = \begin{pmatrix} 0 & 0 & 1 & 0 \\ 0 & 0 & 0 & -1 \\ -1 & 0 & 0 & 0 \\ 0 & 1 & 0 & 0 \end{pmatrix}. \tag{A.2}$$

Appendix B

Fit Functions

B.1 Crystal Ball

The Crystall Ball function was developed by the Crystall Ball collaboration in order to model the detector's response. It is composed of a Gaussian of mean $\bar{x}$ and standard deviation σ joined at $(\bar{x} - \sigma\alpha)$ by a power-law low-end tail of power n. The form of the function is as follows

$$f(x;\alpha,n,\bar{x},\sigma) = N \cdot \begin{cases} \exp -\frac{(x-\bar{x})^2}{2\sigma^2}, & \text{for } \frac{x-\bar{x}}{\sigma} > -\alpha \\ \left(\frac{n}{|\alpha}\right)^n \cdot \exp -\frac{|\alpha|^2}{2} \cdot \left(\frac{n}{|\alpha|} - |\alpha| - \frac{x-\bar{x}}{\sigma}\right)^{-n}, & \text{for } \frac{x-\bar{x}}{\sigma} <= -\alpha \end{cases} \tag{B.1}$$

where N is a normalization factor. A more detailed description can be found in [59].

B.2 Breit-Wigner

The non-relativistic Breit-Wigner function is used to model resonances in the presence of finite detector resolutions. It is defined as

$$\frac{1}{(x-m)^2 + \frac{1}{4}g^2} \tag{B.2}$$

where x, m, and g are parameters.